Michigan Technological University

Digital Commons @ Michigan Tech

Michigan Tech Publications

11-1-2016

MoS2 as a co-catalyst for photocatalytic hydrogen production from water

Bing Han
Michigan Technological University, binhan@mtu.edu

Yun Hang Hu
Michigan Technological University, yunhangh@mtu.edu

REVIEW

MoS$_2$ as a co-catalyst for photocatalytic hydrogen production from water

Bing Han & Yun Hang Hu

Department of Materials Science and Engineering, Michigan Technological University, 1400 Townsend Drive, Houghton, Michigan 49931-1295

Abstract

Solar-to-hydrogen conversion based on photocatalytic water splitting is a promising pathway for sustainable hydrogen production. The photocatalytic process requires highly active, inexpensive, and earth-abundant materials as photocatalysts. As a presentative layer-structured transition metal dichalcogenides, molybdenum disulfide (MoS$_2$) is attracting intensive attention due to its unique electro and photo properties. In this article, we comprehensively review the recent research efforts of exploring MoS$_2$ as a co-catalyst for photocatalytic hydrogen production from water, with emphasis on its combination with CdS, CdSe, graphene, carbon nitride, TiO$_2$, and others. It is shown that MoS$_2$–semiconductor composites are promising photocatalysts for hydrogen evolution from water under visible light irradiation.

Introduction

Global demand for energy is predicted to be more than double by 2050 [1]. If only fossil fuels are exploited to meet this requirement, the content of carbon dioxide in the atmosphere will be more than double, thereby enhancing global warming. Therefore, it is a great challenge to meet the growing energy requirement without contribution to environmental issues. The sun is the only source that is capable of providing enough energy [2]. Sunlight energy, however, is intermittent and requires an efficient storage [1, 3–5]. Sunlight-driven water splitting to produce hydrogen is widely considered as one of the most attractive methods for solar energy storage [6].

The overall water splitting reaction can be expressed as follows:

$$H_2O \rightarrow H_2 + \frac{1}{2}O_2 \quad \Delta G^0_{298K} = 237.1 \, kJ \, mol^{-1} \quad (1)$$

The input energy of this reaction corresponds to a thermodynamic voltage requirement of 1.23 V [7, 8]. Without bias, the conduction band (CB) minimum of semiconductor photocatalyst should be more negative than the H$^+$/H$_2$ redox potential and the valence band (VB) maximum should be more positive than the O$_2$/H$_2$O redox potential. When a photon with energy of $h\nu$ matches or exceeds the band gap energy (E_g) of the semiconductor, an electron in the VB can be excited into the CB, leaving a positive hole in the VB. With the generated electrons, H$_2$ evolution reaction takes place at the cathode, while the generated holes participate in the oxygen evolution reaction at the anode, which are shown below as they occur in acidic electrolyte:

Hydrogen evolution reaction (HER): 2H$^+$ + 2e$^-$ → H$_2$
Oxygen evolution reaction (OER): H$_2$O → $\frac{1}{2}$O$_2$ + 2H$^+$ + 2e$^-$

Fujishima and Honda reported the first photoelectrochemical (PEC) cell for water splitting, in which a rutile TiO$_2$ was used as a photoelectrode and Pt as a counter electrode [9]. Under UV light irradiation on TiO$_2$, O$_2$ was formed at TiO$_2$ surface, while water was reduced to produce H$_2$ at the Pt counter electrode. When heterojunctions of expensive group III–V materials (such as a GaInP$_2$ and

n-p-GaAs junctions in series) were employed as a photoelectrode with a Pt counter electrode, a high energy conversion efficiency of 12.4% was achieved [10]. In this tandem configuration, each semiconductor only needs to supply part of the photovoltage required to electrolyze water and some with smaller band gaps can be used to absorb the visible and near-infrared lights of solar. A low-cost *Z*-scheme tandem device, which is based on two photosystems connected in series, was also developed [11, 12]. A thin film of nanocrystalline WO$_3$ [12] or Fe$_2$O$_3$ [13] serves as the short-wavelength-irradiation absorber where water was oxidized into O$_2$, while dye-sensitized nanocrystalline TiO$_2$ cells absorb long-wavelength-irradiation to generate H$_2$. Recently, it was demonstrated that the activity of silicon photocathodes could be enhanced by depositing hydrogen evolution catalysts on the protected Si surface [13].

Compared to the PEC configuration, a photocatalytic process generally exhibits a low efficiency for overall water splitting due to the back reaction. Pt/TiO$_2$ is one of well-investigated catalysts. However, it works only under UV irradiation and its efficiency for overall water splitting is extremely low. In the 1980s, CdS [14] and WO$_3$ [15] were among few visible light photocatalysts for H$_2$ and O$_2$ evolution. With continuous and intensive efforts, many photocatalyst systems have been developed. For example, an efficient water splitting was achieved using a powdered photocatalyst of NiO/NaTaO$_3$:La under UV irradiation [16]. Furthermore, powdered photocatalyst systems, such as Cr$_x$Rh$_{2-x}$O$_3$/GaN:ZnO [17] and *Z*-scheme systems, such as Ru/SrTiO$_3$:Rh-BiVO$_4$ [18], were developed for visible light water splitting. Besides metal oxide and metal nitride, sulfide solid solution photocatalysts (AgInS$_2$–CuInS$_2$–ZnS) were also demonstrated to be active for H$_2$ evolution under visible light irradiation [19]. Very recently, we reported a highly efficient temperature-induced visible light photocatalytic hydrogen production from water, which exhibited a high photohydrogen yield with a large apparent quantum efficiency (QE) for the entire visible light range at 280°C [20, 21].

Platinum is mostly used with semiconductors as photocatalysts for HER from water due to their negligible overpotential and excellent kinetics. However, because the widespread use of platinum would be limited by its scarcity and high cost [22], it is necessary to develop nonnoble metal alternatives. For example, nickel-based catalysts showed high activity but instability in acidic conditions [23]. Molybdenum is a transition metal that is relatively abundant and therefore much more economical than platinum. Furthermore, MoS$_2$-based materials offer significant advantages for photohydrogen production over noble metal catalysts. Several excellent review articles have been published for the structures, properties, synthesis, and catalytic

performance of MoS$_2$ [24–33]. In this article, we attempt to provide a comprehensive review on MoS$_2$ as a co-catalyst for photocatalytic hydrogen production from water.

Structures and Preparation of MoS$_2$

Crystalline MoS$_2$ occurs in nature as mineral molybdenite. In 1923, Dickson and Pauling took a Laue photograph of mineral molybdenite with the incident beam normal to the basal plane and found it possessed a hexagonal axis and six symmetry planes [34]. In the 1960s, Frindt et al. [35] showed that the micromechanical peeling technique can be employed to obtain thin sheets of MoS$_2$ with thicknesses of 1.2–1.5 nm, corresponding to two molecular layers. In 1980s, efforts were made to obtain single layers of MoS$_2$ using lithium intercalation followed by exfoliation in water [36]. The absence of the (002), (103), and (105) peaks in the X-ray diffraction pattern is characteristic of one-molecule-thick sheets. Furthermore, Koma and Yoshimura [37] obtained a single-layer MoS$_2$ and MoSe$_2$ by van der Waals epitaxy. Frindt et al. carried out a detailed structural investigation of single-layer MoS$_2$ prepared by exfoliation of lithium-intercalated MoS$_2$ powder [38]. So far, three crystal structures were revealed for MoS$_2$. The unique layered structure endows MoS$_2$ with many promising properties, such as anisotropy, chemical stability, and antiphotocorrosion.

Crystal structures of MoS$_2$

As shown in Figure 1, the single layer of MoS$_2$ possesses the Lamellar S–Mo–S structure with a thickness of ~0.7 nm [39]. Each 2D crystal layer of MoS$_2$ consists of a hexagonal plane of Mo atoms and two S atoms of hexagonal planes modulated by covalent interactions in the form of a trigonal prismatic form. Adjacent atomic sandwich units are joint by weak van der Waals forces. The Mo-S length, the crystal lattice constant, and the distance (between the upper and lower sulfur atoms) are 2.4, 3.2, and 3.1 Å, respectively [40, 41]. MoS$_2$ has two main types of phases: 2H and 3R phases. The former contains two layers per unit cell stack in the hexagonal symmetry with trigonal prismatic coordination, and the latter can be described by three layers per unit cell stack in the rhombohedral symmetry with trigonal prismatic coordination [42]. The 2H phase is dominant in nature and more stable than the 3R phase. Furthermore, Frindt and co-workers exploited X-ray diffraction for the detailed structural evaluation of single-layer MoS$_2$ prepared by exfoliation of lithium-intercalated MoS$_2$ powder and discovered the 1T metallic phase, in which Mo atoms are coordinated in an octahedral manner (Fig. 1) [38]. The metallic phase possesses unique electrical properties [43–46]. As a
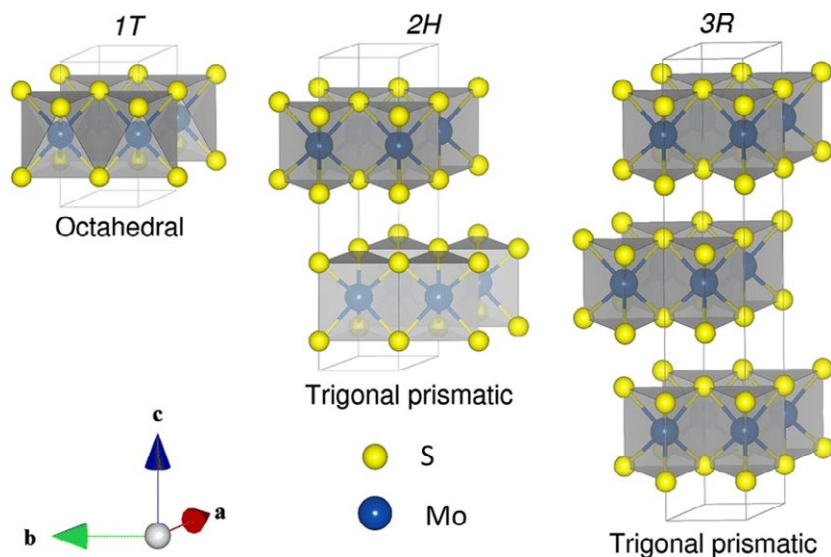
Figure 1. Crystal structure of MoS₂: Octahedral (1T), Trigonal prismatic (2H) and Trigonal prismatic (3R) unit cell structures. Reproduced with permission [47].

metastable structure, the 1T phase can transform into the 2H phase by heating or aging.

Electrical structures of MoS₂

Photocatalysts must possess high stability and suitable energy band structures. MoS₂ has an excellent stability against the photocorrosion in solution due to its antibonding state (formed from an interaction between molybdenum d_z^2, and sulfur p_z orbital at the top of the valence band) [48]. The conduction band position of bulk MoS₂ is slightly more positive than that for the HER, indicating that bulk MoS₂ cannot evolve hydrogen under light illumination without a negative bias or quantum confinement. However, the band gap of MoS₂ varies with the number of its layers [49]. As the thickness of MoS₂ decreased to the size of a monolayer, a transformation from the indirect band gap (1.3 eV) to the direct band gap (1.9 eV) was observed [50–52]. Such an interesting transformation was explained as follows: The VB top edge and the CB bottom edge of MoS₂ are located at the Γ point almost halfway along the Γ-K direction, respectively, which constitutes the indirect band gap transition (Fig. 2) [53, 54]. With decreasing layer number, the bottom edge of the CB moves upward, increasing the overall band gap. Since the CB states at the K point are mainly associated with the Mo *d*-orbitals and relatively unaffected by interlayer interactions, the direct band gap at the K point only increases about 0.05–0.1 eV [55]. The states near the Γ point on the CB that are due to the hybridization between S p_z-orbitals and Mo *d*-orbitals, are strongly dependent on the interlayer interaction. Thus, the bands at Γ are

remarkably affected by decreasing layer number [49, 55]. As a result, for the monolayer, the indirect transition gap is larger than the direct transition gap, and the direct band gap (about 1.9 eV) at K point becomes the smallest gap.

Quantum confinement, which usually affects the band gap in semiconductors was also employed to tune the band gap of MoS₂ and thus its photocatalytic activity. For example, in the visible light-driven photo-oxidation of the organic pollutant molecules phenol and pentachlorobenzene, MoS₂ with size of 8–10 nm exhibited negligible activity, whereas MoS₂ with size of 4.5 nm had reasonable activity [57]. The increased activity was attributed to the quantum confinement giving a lager oxidation potential as a result of the valence band lying at a more positive value.

Synthesis of MoS₂

The synthesis and exfoliation of MoS₂ materials were reviewed elsewhere [58]. Two synthesis strategies were employed: (1) the top-down approach, such as mechanical exfoliation [59, 60], and chemical exfoliation [61–63]; and (2) the bottom-up approach, including chemical vapor deposition on substrates [63, 64] and chemical synthesis [65–67]. MoS₂ has been prepared as a co-catalyst with various methods:

- *Impregnation method* is widely used for the dispersion of nanoparticulate MoS₂ (2H) on photosensitizer (e.g., CdS, TiO₂) for both powdered photocatalysis and PEC processes. For example, MoS₂ on CdS can be prepared
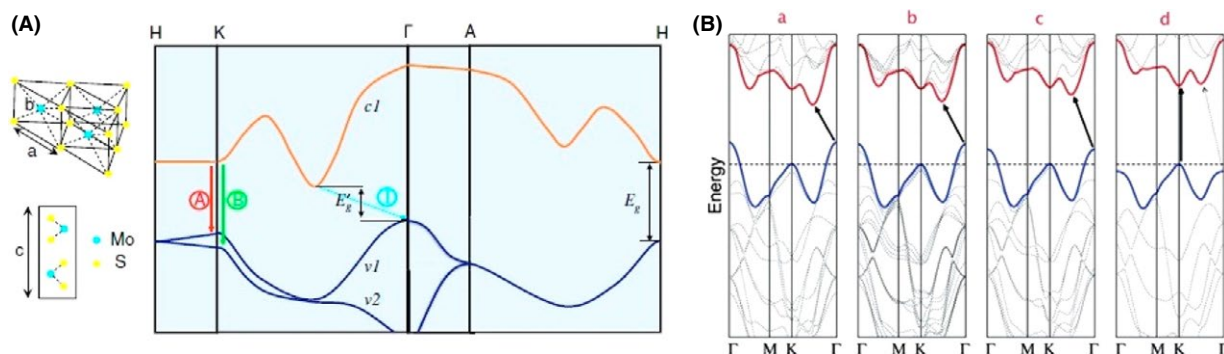
(A) **(B)**

Figure 2. Band structure of MoS$_2$ (A) showing the direct and indirect band gap, as well as the A and B excitons. (B) Transition of the band structure of MoS$_2$ from indirect to direct band gap (a → d). Reproduced with permission [51, 56].

by impregnating CdS with an aqueous solution of (NH$_4$)$_2$MoS$_4$, followed by treatment in H$_2$S flow at high temperature [68].

- *Hydrothermal method* could use low toxic thiourea as a sulfur source to react with molybdenum salt (such as Na$_2$MoO$_4$), together with semiconductor powders [69].
- *Ball-milling method* was employed to mix (NH$_4$)$_2$MoS$_4$ and semiconductor powder in the presence of ethanol, followed by high temperature calcination in inert atmosphere [70].
- *Photodeposition approach* could be used to decorate MoS$_2$ nanocrystals on TiO$_2$ under UV irradiation with (NH$_4$)$_2$MoS$_4$ as precursor in ethanol/water solution [71].
- *Anion exchange reaction* was applied to synthesize MoS$_2$ nanotube photoelectrode from Mo$_3$O$_{10}$(C$_2$H$_{10}$N$_2$) nanowires and L-cysteine by heating at 200°C for 14 h [72].
- *Chemical exfoliation process* was usually exploited to prepare 1T metallic MoS$_2$ catalysts by ion intercalation [73].

More detail for the synthesis of MoS$_2$ co-catalysts will be discussed in the following sections.

MoS$_2$-based Composites as Photocatalysts for the Splitting of Water to H$_2$

A standard photocatalyst for hydrogen evolution consists of platinum and a semiconductor, but platinum is very expensive with a limited source [22]. Therefore, the exploration of nonnoble metal alternatives for platinum is an important topic. Nanostructured nickel phosphide [74], cobalt phosphide [75], and molybdenum sulfides [76] are among the best reported systems with demonstrated high activity for HER, and some of them showed excellent stability under controlled conditions. Furthermore, Mo-based complexes offer significant advantages over noble metal catalysts as co-photocatalysts for H$_2$ production (Table 1).

CdS/MoS$_2$

Cadmium sulfide (CdS), which is an *n*-type semiconductor with a band gap of 2.4 eV, was reported as a visible light active photocatalyst for H$_2$ production 30 years ago [14]. However, CdS suffers photocorrosion during the photo-reaction where CdS can be oxidized by photo-generated holes. To stabilize the CdS nanoparticles, sacrificial electron donors have been employed. Since CdS alone showed very poor catalytic activities for HER, co-catalysts (such as noble metals) are necessary. However, noble metals are expensive with limited source. The earth abundant *p*-type MoS$_2$ is promising as a co-catalyst because of its suitable band structure, high thermal stability, and electrostatic integrity [39, 105]. Furthermore, MoS$_2$ and CdS share the same hexagonal crystalline structure, ensuring that an intimate heterojunction can be formed. Li et al. reported a number of MoS$_2$/CdS systems, in which MoS$_2$ nanoparticles were deposited onto CdS as both a colloidal system and a photocathode [68, 103, 106]. In the colloidal system, electron donors (such as lactic acid, glycerol, ethanol, and methanol) were introduced to inhibit the photocorrosion of CdS. As shown in Figure 3, one can see a higher rate of hydrogen evolution on MoS$_2$/CdS than on metal/CdS, indicating a favorable interaction between MoS$_2$ and CdS [68, 106].

To improve photocatalytic activity, various preparation methods were exploited to engineer nanostructures of MoS$_2$–CdS composites. Chen et al. [70] developed a simple ball-milling method with calcination to prepare MoS$_2$/CdS photocatalysts for visible light-driven H$_2$ evolution. A suitable extent of ball-milling provides a uniform dispersion of MoS$_2$ (prepared from (NH$_4$)$_2$MoS$_4$) on CdS nanoparticles. This intimate contact of heterojunction can facilitate the electron transfer between MoS$_2$ and CdS, resulting in the remarkable increase in H$_2$ evolution rate (Fig. 4A). However, further increasing ball-milling time could cause a gradual decrease in the H$_2$ evolution rate

Table 1. Summary of photocatalytic activity of MoS$_2$-based materials.

Catalyst	Light source	Sacrificial reagent	H$_2$ yield (mmol g^{-1} h^{-1})	Reaction time	Reference
MoS$_2$/CdS					
0.1 g MoS$_2$/CdS	300 W Xe lamp λ > 420 nm	10% lactic acid in water	5.30		[68]
0.1 g MoS$_2$/CdS	300 W Xe lamp λ > 420 nm	10% lactic acid in water	13.15	5 h	[70]
0.05 g MoS$_2$/CdS	300 W Xe lamp λ > 400 nm	Na$_2$S/Na$_2$SO$_3$ aqueous solution	3.84	5 h	[69]
0.02 g CdS/graphene/MoS$_2$	UV lamp 280–320 nm, 500 W	10% lactic acid in water	6.86		[77]
0.2 g MoS$_2$–CdS/γ-TaON hollow composites	300 W Xe lamp λ > 420 nm	0.35 mol L^{-1} Na$_2$S/0.25 mol L^{-1} Na$_2$SO$_3$ aqueous solution	3.14	5 h	[78]
0.02 g 2D MoS$_2$/CdS p-n nanohybrids	300 W Xe lamp λ > 420 nm	10% lactic acid in water	6.85	4 h	[79]
0.05 g rGO/CdS/MoS$_2$	350 W Xe lamp λ > 420 nm (34 mW cm^{-1})	10% lactic acid in water	1.98	5 h	[80]
0.1 g MoS$_2$/CdS	300 W Xe lamp λ > 400 nm	10% lactic acid in water	4.06	5 h	[81]
MoS$_2$/Graphene					
0.02 g Eosin dye Y sensitized MoS$_2$/RGO	300 W Xe lamp λ > 420 nm	15 vol. % TEOA aqueous solution	4.19	6 h	[82]
0.08 g TiO$_2$ NPs/MoS$_2$/graphene	300 W Xe lamp	25 vol. % ethanol in water	2.07	3 h	[48]
0.01 g p-MoS$_2$/n-N-doped RGO	AM 1.5G solar simulator (40–50 mW cm^{-2})	50 vol. % ethanol aqueous solution	0.025	20 h	[83]
0.1 g MoS$_2$/graphene/CdS nanorods	300 W Xe lamp λ > 400 nm	20 vol. % lactic acid aqueous solution	2.32		[84]
0.2 g MoS$_2$/Graphene/CdS	300 W Xe lamp λ > 420 nm	20 vol. % lactic acid aqueous solution	9	5 h	[85]
0.2 g MoS$_2$/graphene	Xe lamp (λ > 390 nm) (1.3 W m^{-2})	15% TEOA aqueous solution with Eosin Y dye	1.21		[86]
0.01 g MoS$_x$C$_y$ (C$_3$)	300 W Xe lamp λ > 420 nm	Triethylamine, water, [Ru(bpy)$_3$] (PF$_6$)$_2$ in acetonitrile	12	16 h	[87]
0.01 g MoS$_x$C$_y$ (C$_3$)	300 W Xe lamp λ > 420 nm	Triethylamine, water, [Ir(pyb)$_2$(bpy)] (PF6) in acetonitrile	19	16 h	[87]
0.01 g CdSe/MoS$_2$	300 W Xe lamp λ > 400 nm (450 mW cm^{-2})	0.1 mol L^{-1} Na$_2$S/0.1 mol L^{-1} Na$_2$SO$_3$ aqueous solution	0.9	300 min	[88]
MoS$_2$/TiO$_2$					
1 g MoS$_2$/SiO$_2$/TiO$_2$	Medium pressure Hg lamp	KOH, water methanol	0.86		[89]
0.03 g MoS$_2$/TiO$_2$	300 W Xe lamp	5% formic acid aqueous solution	0.03	5 h	[71]
0.0016 g MoS$_2$/TiO$_2$	300 W Xe lamp (600 mW cm^{-2})	0.35 mol L^{-1} Na$_2$S/0.25 mol L^{-1} Na$_2$SO$_3$ aqueous solution	1.6		[90]
0.05 g MoS$_2$/TiO$_2$	300 W Xe lamp AM 1.5G filter	20 vol. % methanol aqueous solution	0.12	4 h	[91]
0.2 g MoS$_2$/TiO$_2$	300 W Xe lamp (250–380 nm)	15% methanol aqueous solution	0.75	6 h	[92]
MoS$_2$/TiO$_2$	300 W Xe lamp λ > 420 nm	0.35 mol L^{-1} Na$_2$S/0.25 mol L^{-1} Na$_2$SO$_3$ aqueous solution	0.49	5 h	[93]
MoS$_2$/Carbon nitride					
0.1 g MoS$_2$/g-C$_3$N$_4$	300 W Xe lamp λ > 400 nm	25% methanol aqueous solution	0.231	6 h	[94]
0.02 g MoS$_2$/mesoporous g-C$_3$N$_4$	300 W Xe lamp λ > 420 nm	10 vol. % lactic acid aqueous solution	1.4	5 h	[95]
MoS$_2$/Zn-based material					
0.05 g MoS$_2$/ZnIn$_2$S$_4$	300 W Xe lamp λ > 420 nm	0.5 mol L^{-1} Na$_2$SO$_3$/0.43 mol L^{-1} Na$_2$S aqueous solution	3.06	5 h	[96]
0.1 g MoS$_2$/ZnIn$_2$S$_4$	300 W Xe lamp λ > 420 nm	10 vol. % lactic acid aqueous solution	8.047	5 h	[97]
MoS$_2$/Graphene/ZnS	300 W Xe lamp (125 mW cm^{-2})	0.005 mol L^{-1} Na$_2$S/0.005 mol L^{-1} Na$_2$SO$_3$ aqueous solution	2.26		[98]
MoS$_2$/transition metals or other materials					
Amorphous MoS$_3$ on a CdSe seeded CdS nanorod	450 nm single wavelength (40 mW cm^{-2})	TEOA aqueous solution	100	50 min	[99]

Table 1. (Continued)

| Catalyst	Light source	Sacrificial reagent	H$_2$ yield (mmol g^{-1} h^{-1})	Reaction time	Reference
0.02 g nioblate/graphene/ MoS$_2$	500 W mercury vapor lamp	10% methanol aqueous solution	2.12	2 h	[100]
0.01 g Cr/MoS$_2$/CdS	300 W Xe lamp λ > 420 nm	0.25 mol L^{-1} Na$_2$S/0.35 mol L^{-1} Na$_2$SO$_3$ aqueous solution	38	4 h	[101]
0.01 g Ag/MoS$_2$/CdS	300 W Xe lamp λ > 420 nm	0.25 mol L^{-1} Na$_2$S/0.35 mol L^{-1} Na$_2$SO$_3$ aqueous solution	107	4 h	[101]
0.2 g MoS$_2$/SrZrO$_3$	100 W mercury lamp	0.35 mol L^{-1} Na$_2$S/0.25 mol L^{-1} Na$_2$SO$_3$ aqueous solution	26.55		[102]
MoS$_2$/Sensitizer					
2 g Colloidal MoS$_2$	300 W Xe lamp λ > 420 nm	Ascorbic acid, [Ru(bpy)$_3$](PF$_6$)$_2$ in acetonitrile/methanol	0.21	6 h	[103]
0.001 g MoS$_2$ nanosheet/ TiO$_2$ nanowire with Eosin Y dye	300 W Xe lamp λ > 420 nm	5 vol. % TEOA aqueous solution	16.7	12 h	[104]
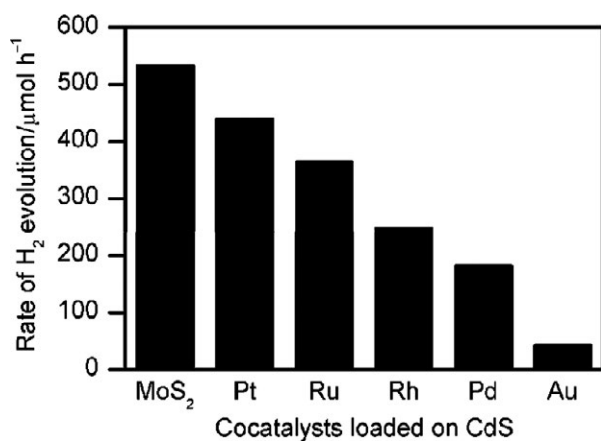
Figure 3. The rate of H$_2$ evolution on CdS loaded with 0.2 wt. % of different co-catalysts. (Xe lamp, 0.1 g catalyst, 10 vol % lactic solution). Reproduced with permission [68].

due to the creation of too many defects, which act as electron-hole recombination centers. The calcination treatment is also important, because it can complete the decomposition of (NH$_4$)$_2$MoS$_4$ to form an effective MoS$_2$ co-catalyst for CdS. Furthermore, increase in calcination temperature can eliminate the defects to improve the crystallinity of photocatalysts, leading to higher photocatalytic activity. However, the calcination at too high temperatures could cause a decrease in surface area and a change in morphology, leading to a remarkable decrease in photocatalytic activity (Fig. 4B). Recently, a hot-injection method was developed to prepare MS$_2$/CdS (M=W or Mo) nanohybrids, in which single-layer MS$_2$ nanosheets with lateral size of 4–10 nm grew on the Cd-rich (0001) surface of wurtzite CdS nanocrystals. A large number of edge sites in the MS$_2$/CdS nanohybrids are active sites for HER. The photocatalytic performances over MoS$_2$/ CdS nanohybrids reached 1472 μmol h^{-1} g^{-1} hydrogen yield for HER under visible light irradiation (>420 nm), which is about 12 times that of pure CdS. Furthermore, the MS$_2$/CdS nanohybrids showed an enhanced stability, namely, after a reaction of 16 h, 70% of catalytic activity still remained.

A green hydrothermal method was explored for the synthesis of MoS$_2$/CdS photocatalysts for H$_2$ production under visible light irradiation [69]. This approach, which uses low toxic thiourea as a sulfur source to react with Na$_2$MoO$_4$ at 200°C, is better than traditional methods, which are based on an annealing process at relatively high temperature (above 400°C) with toxic H$_2$S as a reducing agent. The H$_2$ evolution rate of the MoS$_2$/CdS is 17 times larger than that of CdS alone. The morphologies of obtained MoS$_2$/CdS samples were feather shaped (Fig. 5A). Furthermore, transmission electron microscopy (TEM) images showed the layer of flocculent material coated on the surface of CdS catalyst (Fig. 5B), indicating that MoS$_2$ was uniformly dispersed on CdS [81].

The coupling of p-type MoS$_2$ and n-type CdS to form p-n junctions at heterostructure interfaces was found helpful for enhancing photo-generated electron-hole separation. Mott–Schottky (M-S) plot of CdS film showed a positive slope in the linear region, indicating an n-type characteristic. In contrast, MoS$_2$ film exhibited p-type behavior, reflected by a negative slope in its M-S plot [107]. The p-n junctions of MoS$_2$/CdS could accelerate the effective separation of photo-generated carriers by the internal electrostatic field at the junction interface. The excited electrons on the conduction band of the MoS$_2$ transfer to that of CdS and further to the counter electrode to produce hydrogen (Fig. 6). Simultaneously holes are transferred to VB of MoS$_2$ and accumulate
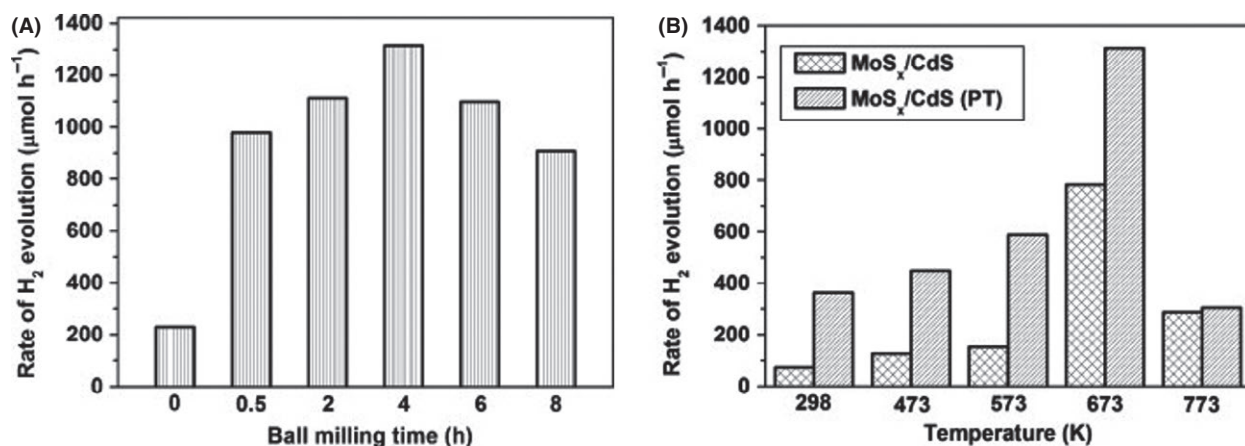
Figure 4. (A) The H$_2$ evolution rate of 0.9 mol% MoS$_2$/CdS (pretreated) photocatalysts (prepared with different ball-milling time followed by calcining at 673 K for 2 h) under visible light (λ > 420 nm) with lactic acid as electron donor. (B) The H$_2$ evolution rate based on 0.9 mol% MoS$_x$/CdS and 0.9 mol% MoS$_x$/CdS (pretreated) photocatalysts (prepared by calcining the (NH$_4$)$_2$MoS$_4$/CdS and (NH$_4$)$_2$MoS$_4$/CdS (pretreated) precursors at different temperatures for 2 h) under visible light (λ > 420 nm) with lactic acid as a sacrificial reagent. Reproduced with permission [70].
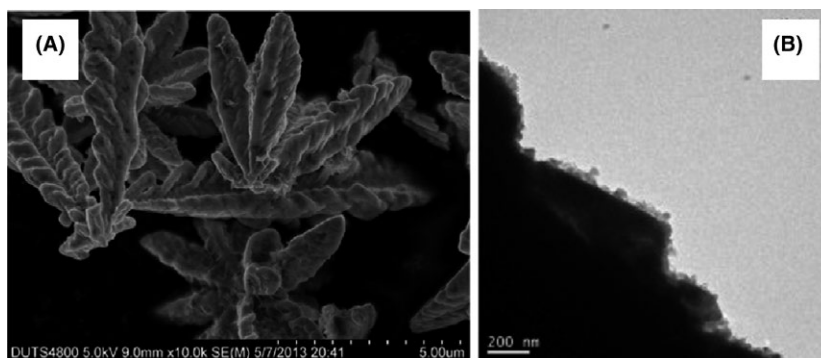

Figure 5. (A) SEM image of feather-shaped MoS$_2$/CdS samples. Reproduced with permission [65]. (B) TEM images of MoS$_2$/CdS catalyst synthesized by loading 2.0 wt. % MoS$_2$ on CdS. Reproduced with permission [81].
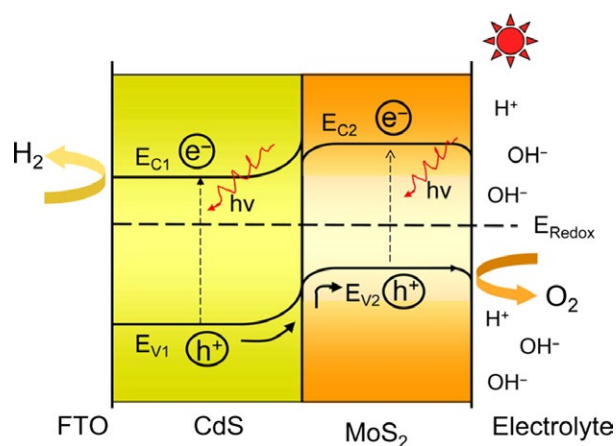

Figure 6. Formation of a *p-n* junction when MoS$_2$ contacts CdS. Reproduced with permission [107].

there, which inhibit photocorrosion of CdS and thus enhance its photostability. Furthermore, the effect of MoS$_2$/CdS *p-n* heterojunctions on PEC was evaluated. MoS$_2$/CdS *p-n* heterojunction films, which were prepared by electrodeposition followed by chemical bath deposition, showed much higher visible light PEC activity and higher stability for water splitting than pure CdS film [107]. The highest photocurrent of the MoS$_2$/CdS film was seven times higher than that of the pure CdS film. The improved PEC performance of the MoS$_2$/CdS heterojunction film was attributed to the enhanced visible light absorption by MoS$_2$ and the formation of a *p-n* junction between CdS and MoS$_2$. The IPCE measurement revealed that MoS$_2$/CdS heterojunction not only contributed to the improvement of the electron-injection efficiency in the CdS absorption region (λ < 510 nm), but also broadened the utilization range of the solar spectrum to red light

region (λ > 510 nm). In contrast, MoS$_2$ or CdS alone exhibited a very low photocatalytic activity. A comparison of PL spectra between CdS and MoS$_2$/CdS indicates effective charge transfer between *n*-type CdS and *p*-type MoS$_2$ under illumination, which results from the lower recombination probability of photo-generated electrons and holes. Furthermore, the holes transferred from CdS to MoS$_2$ prevented the photocorrosion of CdS, leading to better stability. 2D MoS$_2$ nanosheets were also utilized to fabricate 2D MoS$_2$/CdS with a sandwich-like *p-n* heterojunction through a one-pot solvothermal process [79]. Transient photocurrent tests revealed that the photocurrent is enhanced ~4.5-fold compared with that of pure CdS nanoparticles.

Recently, other semiconductor materials were explored to combine with MoS$_2$–CdS composites for the improvement of photocatalytic activity [78]. Three-dimensional MoS$_2$–CdS–γ-TaON hollow composites were successfully synthesized by anchoring MoS$_2$/CdS nanocrystals on the surfaces of γ-TaON hollow spheres with a hydrothermal approach [78]. The photo-excited electrons in the CB of CdS can migrate and be injected into TaON, followed by transfer to the MoS$_2$ nanosheets to generate H$_2$, which inhibits the charge carrier recombination. Even without a noble-metal co-catalyst, the hollow-structured MoS$_2$-CdS-γ-TaON with 1 wt. % MoS$_2$/CdS co-catalyst (0.2 wt. % MoS$_2$) decorated on its surface produced a high photocatalytic H$_2$ production rate of 628.5 μmol h^{-1}, which is about 70 times higher than that of Pt on pristine TaON. The PEC performance was examined for the system with TiO$_2$/CdS/ZnS as a photoelectrode and TiO$_2$/CdS/MoS$_2$

heterointerface as a counter electrode (Fig. 7) [108]. This tandem electrode configuration showed higher hydrogen fuel generation of 1.47 mL h^{-1} cm^{-2} at 1 V versus RHE applied potential under visible light, which is 1.5 times higher than that using Pt as a counter electrode. Furthermore, 1T MoS$_2$ sheet passivation at the TiO$_2$/CdS interface could reduce charge recombination with the electrolyte through uncovered CdS sites on TiO$_2$.

In summary, a promising efficiency of photocatalytic H$_2$ production from water splitting under visible light irradiation has been achieved over MoS$_2$–CdS composites. This can be attributed to the matched energy band alignment, *p-n* heterojunction, and uniform dispersion of co-catalyst, which promotes the charge transfer and suppresses the photoelectron/hole recombination.

CdSe/MoS$_2$

Bulk CdSe semiconductor does not have photocatalytic activity for HER, even with sacrificial electron donors, because its conduction band is below the water reduction potential. However, reducing thickness of CdSe nanomaterial can cause strong quantum confinement, leading to a larger band gap and higher conduction band potential. Nano-CdSe possesses a raised CB flat band potential (from −0.10 V to −0.55 V vs. NHE) that results from the increased band gap (from 1.7 to 2.7 eV) [88]. Under visible light irradiation, this quantum confined CdSe-nanoribbons exhibited an attractive H$_2$ production rate from aqueous sodium sulfite/sulfide solution with a quantum efficiency of 9.2% at 440 nm, whereas bulk CdSe is not active for
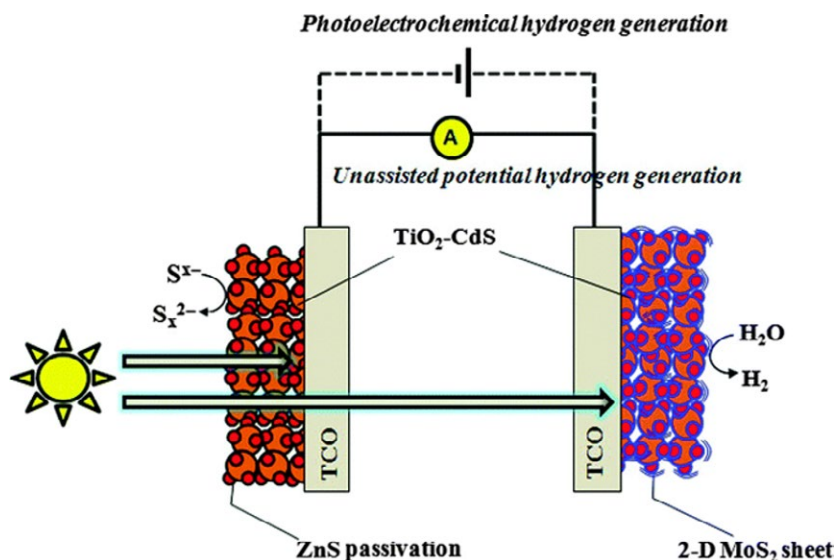

Figure 7. Schematic illustration of the double-sided photoelectrode with TiO$_2$/CdS/ZnS (anode) and TiO$_2$/CdS/MoS$_2$ electrodes (cathode). Reproduced with permission [108].

the reaction. Furthermore, the chemical linking of the CdSe nanoribbons to MoS$_2$ nanoplates increased the activity by almost four times. Cyclic voltammetry reveals that such an enhancement by the MoS$_2$ nanoplates was due to a decrease in the H$_2$ evolution overpotential.

Microwave-deposited MoS$_3$ on CdSe-seeded CdS nanorode was investigated as light harvester (Fig. 8) [99]. The CdSe/CdS nanorod heterostructure could control the pathways of charge migration where photo-generated holes are spatially confined to CdSe core and electrons can delocalize over the entire structure. This heterogeneous spatial distribution, which is the result of the staggered band alignments from CdSe and CdS (that are controlled by seed and rod diameters), decreased electron-hole overlap and increased the exciton lifetime with increasing the rod length or decreasing the seed diameter. Deposition of MoS$_3$ thin film on CdSe/CdS nanorods was demonstrated as a photocatalytic active system for H$_2$ generation, namely, yield of 100 mmol h^{-1} g^{-1} of H$_2$ was obtained over the catalyst of MoS$_3$-coated 60 nm CdS rods containing 2.8 nm CdSe seeds, leading to an apparent quantum efficiency of 10% at 450 nm light. In contrast, irradiation of a solution of MoS$_3$ or as-synthesized CdSe/CdS nanorods alone in water showed a negligible rate for H$_2$ production. Therefore, one can concluded that intimate contact between the MoS$_3$ layers and the CdSe/CdS nanorods is vital for efficient charge transfer and thus beneficial for efficient photocatalytic H$_2$ production. However, the stability test showed a decrease in H$_2$ production over time, which was attributed to the gradual dissolution of MoS$_3$ from the surface of the rods.

Graphene/MoS$_2$

Graphene, a single layer of sp^2-bonded carbon atoms tightly packed into a two-dimensional honeycomb structure, has attracted a lot of attention since its discovery in 2004 [109, 110]. Especially, graphene possesses an excellent mobility of charge carriers at room temperature (2×10^5 cm^2 V^{-1} sec^{-1}) and a high theoretical surface area (~2600 m^2 g^{-1}) [111]. Those unique properties make graphene an efficient electron acceptor to enhance the photo-induced charge transfer and to inhibit the backward reaction by separating the evolution sites of hydrogen and oxygen. MoS$_2$ itself shows very low HER due to its low surface area and insufficient charge separation. However, the combination of MoS$_2$ with graphene as catalysts is very promising for solar hydrogen generation, because graphene can provide a channel for charge transport and promote the growth of highly dispersed MoS$_2$ nanoparticles on it. The most widely used procedure for the preparation of MoS$_2$–graphene composites is the mixing of presynthesized graphene oxide (GO) with molybdate salts, which are hydrotreated in autoclave in the presence of a sulfur containing compound, typically thiourea [73, 82]. It was reported that, in the presence of graphene during the solvothermal process, MoS$_2$ quantum dots (QD) instead of layered MoS$_2$ nanosheets were formed [112]. The formation of MoS$_2$ QDs was attributed to the interactions between functional groups on GO sheets and Mo precursors in a suitable solvent environment. No MoS$_2$ QDs were obtained in the process without GO.

The combination of MoS$_2$ and reduced GO (RGO) sheets was reported in application of water electrolysis where a low over potential of 0.1 V and a small Tafel slope ~41 mV per decade were showed [113]. In contrast, free MoS$_2$ particles or RGO alone exhibited little HER activity. Very recently, MoS$_2$–graphene composites were explored for photocatalytic and PEC H$_2$ evolution. In most cases, the MoS$_2$/RGO composite was coupled with light absorber such as semiconductors or molecular dyes for
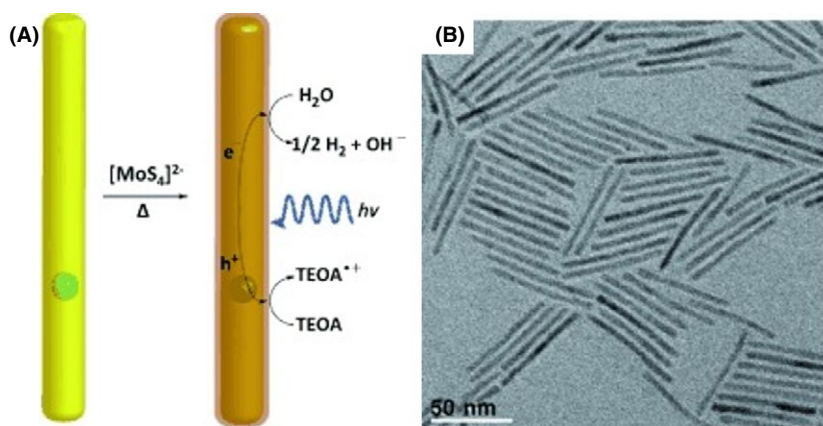

Figure 8. (A) MoS$_3$ deposition on a CdSe-seeded CdS nanorod, with photocatalytic H$_2$ production in the visible light range using triethanolamine (TEOA) as a sacrificial reagent. (B) Bright-field TEM image of CdSe-seeded CdS nanorods (length 60 nm). Reproduced with permission [99].

HER. For co-deposition of Eosin Y dye and the MoS$_2$ nanoparticles on the RGO nanosheets as a photocatalyst, the RGO sheets not only provide a confined substrate for the growth of limited-layer MoS$_2$ (a co-catalyst with a large number of exposed catalytic sites), but also form the interconnected conductive networks for efficiently transferring photo-generated electrons from excited dye to the catalytic active sites of MoS$_2$ [82]. This can suppress the electron-hole recombination and enhance the photocatalytic efficiency of HER. As a result, a greatly improved HER activity compared to that of the pristine MoS$_2$ was achieved, namely, a high apparent quantum efficiency of 24.0% at 460 nm was obtained over an Eosin Y-sensitized MoS$_2$/RGO photocatalyst. However, the MoS$_2$/RGO system showed no photocatalytic activity in the absence of a photosensitizer (Eosin Y dye), indicating that MoS$_2$ provided reaction sites for HER, but did not harvest solar energy.

The photocatalytic activity for H$_2$ evolution was obtained using MoS$_2$/graphene hybrid as a co-catalyst on TiO$_2$ semiconductor nanocrystals [48]. The photo-generated CB electrons of TiO$_2$ can easily migrate into the graphene sheets because the graphene/graphene$^-$ redox potential is slightly lower than the CB of TiO$_2$. Such charge migration from TiO$_2$ to the MoS$_2$–graphene composite could efficiently inhibit charge recombination, improve interfacial charge transfer, and increase active adsorption sites and photocatalytic reaction centers. A high H$_2$ production rate of 165.3 μmol h^{-1} was achieved when the content of MoS$_2$/graphene co-catalyst is 0.5 wt. % and the content of graphene in this co-catalyst is 5 wt. %. The quantum efficiency reached 9.7% at 365 nm in water/ethanol mixture solution, which is 39 and four times larger than those on TiO$_2$ alone and TiO$_2$ with MoS$_2$ co-catalyst, respectively. This impressive HER reaction was attributed to the high mobility of electrons on the graphene sheets and the highly active nanoscale MoS$_2$ as a result of the quantum-confinement effect.

Without additional light harvester, the combination between nanoplatelet p-MoS$_2$ and nitrogen-doped n-RGO can create significant photocatalytic activity for HER in the wavelength range from ultraviolet light through the near-infrared light [83]. MoS$_2$ acts not only as a catalytic site but also as a photocenter for absorbing solar light to generate charge carriers. The quantum confinement of the nano-sized MoS$_2$ enlarges its band gap and thus makes it thermodynamically possible for water reduction. The thin nanoplatelet geometry of MoS$_2$ can increase the edge sites and the contact area with the RGO sheets. Furthermore, nitrogen-doped n-type RGO nanosheets also act as a support for the growth of p-type MoS$_2$ nanoplatelets to form many nanoscale p-n junctions on each RGO nanosheet. 24.8 μmol g^{-1} h^{-1} was achieved by p-MoS$_2$/n-RGO junction under simulated solar light irradiation in the water/ethanol mixture solution, whereas the MoS$_2$–RGO composite without nitrogen-doping has only 7.4 μmol g^{-1} h^{-1} (Fig. 9). Furthermore, MoS$_2$ alone has negligible photocatalytic activity due to its insufficient charge separation. In the MoS$_2$–RGO composite, the RGO increases the energy conversion efficiency as a passive charge extraction layer. When a nanoscale p-n junction is formed in the MoS$_2$–n-RGO composite, the space charge layer creates a built-in electric field and separates the electrons and holes upon light illumination.

Single-layer 1T-MoS$_2$ and few-layer 2H-MoS$_2$ with heavily nitrogenated RGO (N content ca. 15%) showed excellent performance in the production of H$_2$ under visible light illumination [73]. Nitrogen incorporation in graphene could improve the catalytic activity of the composite with 2H-MoS$_2$ layers since it enhances the electron donating ability of the graphene. Furthermore, for photocatalytic process with water (40 mL) and triethanolamine (15% v/v; 8 mL) as a sacrificial, the composite materials were sensitized by Eosin Y as catalysts. The yield of H$_2$ for nitrogen-doped RGO–2H-MoS$_2$ composite (10.8 mmol g^{-1} h^{-1}) is nearly 3.5 times higher than that found with unmodified RGO/2H-MoS$_2$ (Fig. 10A) and about 200 times higher than 2H
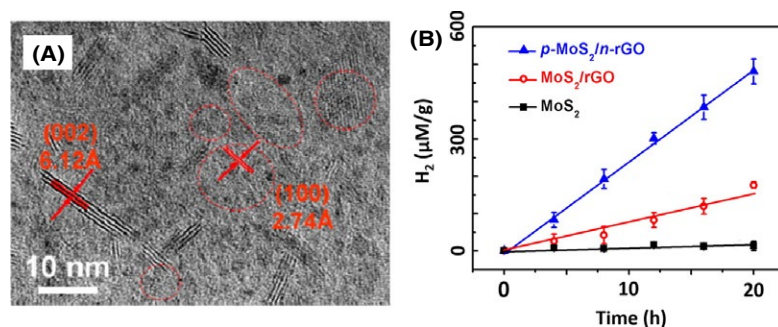

Figure 9. (A) HRTEM image of the p-MoS$_2$/n-rGO. (B) Hydrogen generated by pure MoS$_2$, the MoS$_2$/RGO, and the p-MoS$_2$/n-RGO photocatalysts. Reproduced with permission [83].
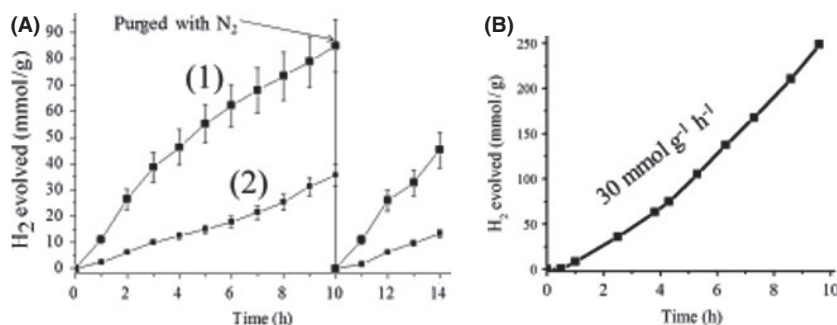
Figure 10. (A) Time course of H$_2$ evolved by (1) Nitrogen-doped RGO-MoS$_2$ and (2) RGO-MoS$_2$ per gram of catalyst. After 10 h of H$_2$ evolution, the vessel was purged. The rate of H$_2$ evolution remains constant after purging. (B) Time course of H$_2$ evolved by freshly prepared 1T-MoS$_2$. Reproduced with permission [73].

MoS$_2$ alone. In contrast, 1T phase of MoS$_2$ showed highly efficient for photocatalytic HER even without graphene due to its metallic conducting property. The H$_2$ yielding of 1T-MoS$_2$ prepared by Li-intercalation of bulk MoS$_2$ followed by exfoliation in water is as high as 30 mmol g^{-1} h^{-1} (Fig. 10B), which is 600 times higher than that of the few layer 2H-MoS$_2$.

From the above discussion, one can conclude that graphene is an active component in photohydrogen production system, which can improve all three vital steps in photocatalysis: charge separation, migration, and recombination. The MoS$_2$/Graphene heterostructure is a promising candidate for the development of efficient visible light photocatalysts for H$_2$ evolution, which contains only earth-abundant, nontoxic, and inexpensive materials.

MoS$_2$/Carbon nitride

Graphitic carbon nitride (g-CN), a polymeric melon semiconductor with a layered structure analogous to graphite, meets the essential requirements as a sustainable solar energy transducer for water redox catalysis. These requirements include being abundant, highly-stable, and responsive to visible light [114]. g-CN has a suitable electronic structure (E_g = 2.7 eV, CB at −0.8 V and VB at 1.9 V vs. RHE) covering the water-splitting potentials [115]. However, g-CN, which alone showed very poor photocatalytic activities, relies on co-catalysts to provide active sites for HER. MoS$_2$ and g-CN have similar layered structures, which would minimize the lattice mismatch and facilitate the planar growth of MoS$_2$ slabs over the g-CN surface [116, 117]. A thin layer can reduce the light blocking effect of the co-catalyst to improve the light absorption of g-CN. Importantly, the more negative position of CB in g-CN than in MoS$_2$ provides the possibility of the directional migration of photo-generated electrons from g-CN to MoS$_2$, while keeping sufficient chemical potential in the electrons for water reduction

at active sites of MoS$_2$ [118]. Therefore, the combination of MoS$_2$ and g-CN can facilitate the charge separation, increase the lifetime of the photo-generated electron/hole pair, and lower activation barriers for H$_2$ or O$_2$ evolution. Namely, MoS$_2$ is a promising co-catalyst for the g-CN photocatalyst.

An organic–inorganic-layered heterojunctions for photocatalytic hydrogen production were obtained by gas-controlled growth of thin-layered MoS$_2$ on a mesoporous g-CN (mpg-CN) surface [95]. As the content of mpg-CN increased for the MoS/mpg-CN catalyst, the rate of photo hydrogen evolution increased to reach a maximum at about 0.2 wt. % MoS$_2$ content and then decreased. The activity decrease at large MoS$_2$ contents is due to the serious shielding effect. Furthermore, thin-layered MoS$_2$ can reduce the poor charge transport from layer to layer and shorten the electron transport time and distance, leading to the efficient utilization of photo-generated electrons for hydrogen production. The best performance of 0.2 wt. % MoS$_2$/mpg-CN showed an apparent quantum yield of 2.1% measured at 420 nm with lactic acid as an electron donor. The hydrogen evolution rate over 0.5 wt. % MoS$_2$/mpg-CN reached 1.03 mmol h^{-1} g^{-1} which is higher than that of 0.5 wt. % Pt/mpg-CN (0.24 mmol h^{-1} g^{-1}) under visible light. In addition, PEC activity of MoS$_2$–g-CN composite was also tested, revealing that 0.5 wt. % MoS$_2$/g-C$_3$N$_4$ sample exhibited the highest catalytic activity with a H$_2$ evolution rate of 0.23 mmol h^{-1} g^{-1}, which is 11.3 times higher than that of g-C$_3$N$_4$ without MoS$_2$ [94].

Ternary g-CN/GO/MoS$_2$ hybrid photocatalyst were synthesized by noncovalent doping of graphite-like carbon nitride (g-CN) with ultrathin GO and MoS$_2$ nanosheets using a facile sonochemical method [119]. In the hybrid, layered MoS$_2$ and GO nanosheets with a large surface area enhance light absorption to generate more photoelectrons [120]. Furthermore, it possesses binary *p-n* heterojunctions at the g-CN/MoS$_2$ and g-CN/GO interfaces,

which can promote charge separation and transfer of electron-hole pairs. As a result, the ternary hybrid photocatalyst exhibits improved PEC and photocatalytic activities under visible light irradiation compared to other reference materials.

In summary, the g-C$_3$N$_4$–MoS$_2$ composite photocatalysts can be synthesized with a facile impregnation method. The favorable electron transfer from g-C$_3$N$_4$ to well dispersed MoS$_2$ layers can inhibit charge recombination and enhance the H$_2$ evolution activity under visible light irradiation.

MoS$_2$/TiO$_2$

As one of the most investigated functional material in semiconductor photocatalysis, titanium dioxide (TiO$_2$) has been widely used for photocatalysis due to its excellent photocatalytic properties of nontoxicity, effectiveness, low cost, and chemical stability [121]. Nevertheless, TiO$_2$ has a band gap larger than 3.0 eV and thus cannot absorb visible light. The employment of earth abundant MoS$_2$ as co-catalyst and photosensitizer has become an attractive strategy to increase solar energy harvesting and photocatalytic activity for TiO$_2$. Cyclic voltammograms (CV) measurements revealed that TiO$_2$ modified with 1.0 wt. % MoS$_2$ can reduce hydrogen reduction overpotential, thereby enhancing photocatalytic activity (Fig. 11) [91]. Furthermore, smaller Nyquist radii of the MoS$_2$–TiO$_2$ composite than that of TiO$_2$ under UV light irradiation indicate that the doping of MoS$_2$ into TiO$_2$ led to an efficient separation of the photo-generated electrons and holes [92].
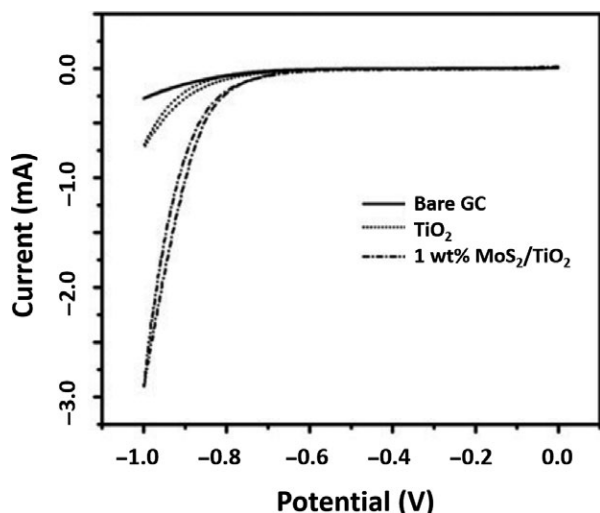

Figure 11. Cyclic voltammograms of bare glassy carbon, pure TiO$_2$, and 1.0 wt. % MoS$_2$/TiO$_2$ in 0.5 mol L^{-1} H$_2$SO$_4$ versus Ag/AgCl at a scan speed of 20 mV sec^{-1}. Reproduced with permission [91].

Various methods were employed to load MoS$_2$ on TiO$_2$, including hydrothermal reaction [90, 91, 93], photodeposition [71, 122], and mechanochemistry [92]. Furthermore, different shapes of TiO$_2$ were employed as templates for the synthesis, such as nanobelt [90], nanowire [104], and nanofibers [93]. It was found that TiO$_2$ nanobelts used as a synthetic template could inhibit the growth of MoS$_2$ crystals along the c-axis, resulting in a few-layer MoS$_2$ nanosheet coating on the TiO$_2$ nanobelts [90]. Small TiO$_2$ nanoparticles possess a short diffusion distance of electron-hole pair, leading to efficient interfacial electron transfer from TiO$_2$ nanoparticles to MoS$_2$ surface [91]. Porous TiO$_2$ nanowire hybrid nanostructures can increase surface area and thus provide more chances to expose the edges of the MoS$_2$ nanosheets to the reactants [104].

The MoS$_2$ content in the MoS$_2$–TiO$_2$ composite could affect its photocatalytic performance. Zhou et al. [90] demonstrated that the optimal MoS$_2$ loading is 50 wt. %, leading to a hydrogen production rate of 1.6 mmol h^{-1} g^{-1}. This happened because too low loading of MoS$_2$ suffers an insufficient visible light absorption, whereas the excessive loading of MoS$_2$ can block the photoelectron transfer between the core part of the TiO$_2$ nanobelt and the shell part of MoS$_2$ nanosheets. It was suggested that the contact between the light absorber and MoS$_2$ is crucial for the electron transfer between two components [68]. Vertically standing single or few-layer MoS$_2$ nanosheets on porous TiO$_2$ nanofibers (TiO$_2$@MoS$_2$) were successfully prepared via a simple hydrothermal reaction [93]. Due to plenty of pores in the TiO$_2$ nanofibers, the MoS$_2$ nanosheets vertically grew from the inside to the outside, and the growth mode of the MoS$_2$ nanosheets rooting into the TiO$_2$ nanofibers endowed not only intimate contact between the TiO$_2$ and MoS$_2$ for fast electrons transfer, but also high structural stability of TiO$_2$@MoS$_2$. The vertical orientation of MoS$_2$ nanosheets enables the active edge sites of MoS$_2$ to be maximally exposed. Without using an expensive Pt co-catalyst, the TiO$_2$@MoS$_2$ heterostructure achieved high photocatalytic H$_2$ production rates of 1.68 and 0.49 mmol h^{-1} g^{-1} under UV-vis and visible light illumination, respectively. In addition, the TiO$_2$@MoS$_2$ catalyst exhibited a high durability as evidenced by the invariable H$_2$ production rate after continuous illumination over 30 h.

In conclusion, tuning TiO$_2$ nanostructure can improve photocatalytic H$_2$ production rate of MoS$_2$–TiO$_2$ composite by increasing surface area and deceasing electron-hole pair diffusion distance. The TiO$_2$–MoS$_2$ hybrid nanostructure of the composite possesses the intimate interaction between MoS$_2$ and TiO$_2$ and the superior structure stability of the MoS$_2$–TiO$_2$ composite, leading to enhanced photocatalytic activity.

MoS$_2$ with Zn-based materials

Zn-related sulfides have shown remarkable versatility of fundamental properties and important applications. Bulk ZnS has a large band gap of ~3.72 eV for cubic zinc blende and ~3.77 eV for hexagonal wurtzite ZnS. It is well known that ZnS is an attractive photocatalyst due to its rapid photogeneration of electron-hole pairs; its highly negative potentials of CB (about −0.91 vs. SHE) results in superior HER activity [123, 124], even without any assistance of noble metal co-catalysts [125]. However, ZnS is unstable in aqueous solutions where it suffers anodic photocorrosion with the formation of sulfur and/or sulfate ions. Furthermore, the rapid electron-hole recombination also limits its practical application. To solve those issues, graphene and MoS$_2$ nanosheets were exploited to modify ZnS nanoparticles (Fig. 12) [98]. The ZnS–graphene–MoS$_2$ nanocomposites exhibited significantly enhanced photocatalytic activity for H$_2$ evolution from water splitting. When the ZnS–graphene–MoS$_2$ nanocomposite contained 0.25 wt. % graphene and 2 atom% MoS$_2$, it exhibited a high H$_2$ evolution rate of 2258 μmol h^{-1} g^{-1}, which is about two times that of ZnS alone under a 300 W Xe lamp in Na$_2$S/Na$_2$SO$_3$ aqueous solution. This can be attributed to the synergistic effect of co-catalysts, namely, graphene serves as an excellent electron acceptor and transporter, and MoS$_2$ nanosheets provide a source of active sites.

ZnIn$_2$S$_4$ is a ternary chalcogenide with unique properties, such as a suitable band gap (2.34–2.48 eV) corresponding to the visible light absorption, low toxicity, considerable chemical stability, and facile preparation process [126]. ZnIn$_2$S$_4$ exhibits two distinct polymorphs based on cubic and hexagonal lattices. Both MoS$_2$ and hexagonal ZnIn$_2$S$_4$ possess a similar layered structure, which might allow MoS$_2$ to easily grow on the ZnIn$_2$S$_4$ surface. The conduction band position of hexagonal ZnIn$_2$S$_4$ (−1.1 eV vs. NHE) is more negative than that of MoS$_2$ (−0.5 and −0.9 vs. NHE [127]), providing a possibility for the transfer of photo-generated electrons from ZnIn$_2$S$_4$ to MoS$_2$. The electrons transferred to CB of quantum confined MoS$_2$ still maintain enough chemical potential for HER reaction. Furthermore, the MoS$_2$/ZnIn$_2$S$_4$ nanocomposite can be synthesized by impregnating ZnIn$_2$S$_4$ with (NH$_4$)$_2$MoS$_4$ aqueous solution, followed by high-temperature treatment in H$_2$S flow [96]. It can also be prepared via an in situ photo-assisted deposition process [97]. The photocatalytic activity of the MoS$_2$–ZnIn$_2$S$_4$ nanocomposite is comparable to that of Pt/ZnIn$_2$S$_4$ and 10 times higher than that of pure ZnIn$_2$S$_4$ [96, 97]. This can be explained by the intimate contact between ZnIn$_2$S$_4$ and MoS$_2$, which promotes the formation of junctions between the two components to improve the charge separation and prolong the mean lifetime of the electron-hole pairs. In addition, the MoS$_2$ in the MoS$_2$–ZnIn$_2$S$_4$ nanocomposite possesses an amorphous state, in which there are many defect sites that can act as adsorption sites for hydrogen atoms [96].

In summary, the combination of Zn-based semiconductors (such as ZnS and ZnIn$_2$S$_4$) with MoS$_2$ can create promising photocatalysts for H$_2$ evolution under visible light irradiation, which is due to their similar layered structures, favorable electron transfer at the heterojunction interface, and the defect sites over MoS$_2$ which act as adsorption site for hydrogen atoms.

MoS$_2$ with transition metals or other metals

Nakagawa et al. [100] prepared single molecular sheets of niobate (K$_4$Nb$_6$O$_{17}$) by a hydrothermal approach using niobium ethoxide with the aid of triethanolamine (TEOA) as a structural modifier (Fig. 13). The highly stable molecular entities against self-assembly allows them to mix
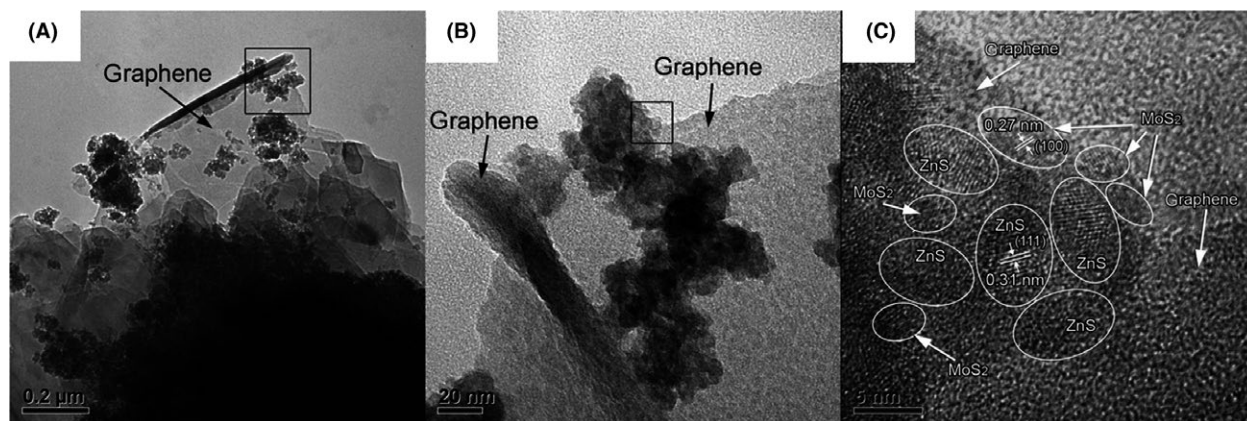
Figure 12. Typical TEM (A) and (B) and HRTEM images (C) of ZnS/Graphene/MoS$_2$, where (B) is the detail of the square frame in (A) and (C) is that in (B). Reproduced with permission [98].
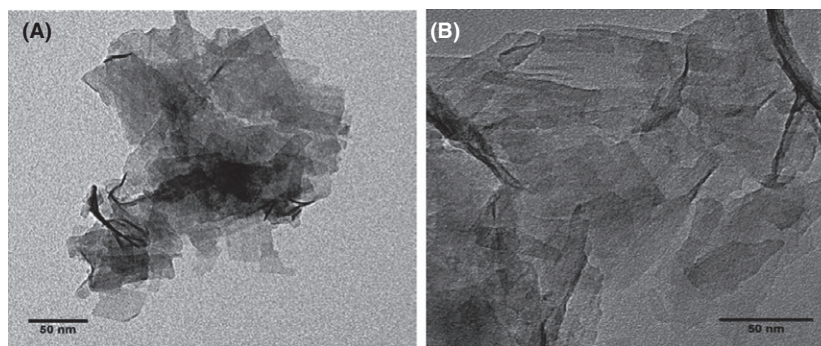
Figure 13. (A) TEM image of niobte/TEOA and (B) HRTEM image of discrete niobate/TEOA single molecular sheets. Reproduced with permission [100].
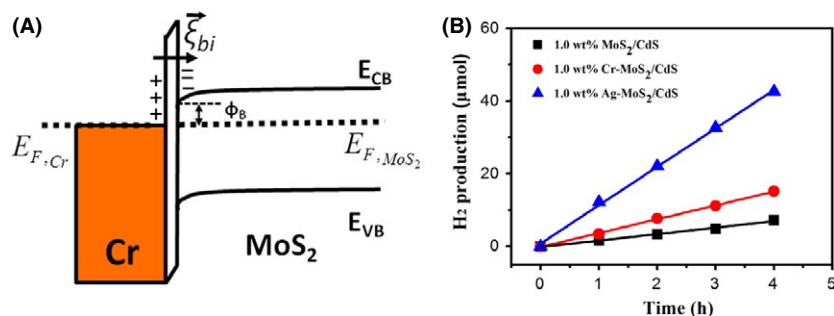

Figure 14. (A) Energy band-edge alignment of Cr-MoS$_2$ hybrid structure. $E_{F,Cr}$ and $E_{F,MoS2}$ are the Fermi Levels of Cr and MoS$_2$, respectively. Φ_B is the electron barrier potential in the hybrid Cr–MoS$_2$ system. E_{CB} and E_{VB} are the conduction and valence band-edges of MoS$_2$, respectively. A thin interfacial layer is inserted between Cr and MoS$_2$ to indicate a nonepitaxial contact. (B) The H$_2$ production as a function of irradiation time. As co-catalysts combined with photocatalyst of CdS, the plots represent 1.0 wt. % Cr–MoS$_2$ (in red), 1.0 wt. % Ag–MoS$_2$ (in blue), and 1.0 wt. % MoS$_2$ (in black). Reproduced with permission [101].

well with other colloids and facilitates their extensive electronic interactions. The 2D niobate molecular sheets can absorb light and generate excited electrons and holes under UV irradiation. MoS$_2$ has a lower conduction band position than those of niobate, but its edge sites can offer lower activation energy for H$_2$O reduction while conjugated graphene acts as an electron transfer mediator. A rapid electron transfer from niobate nanosheets to MoS$_2$ through the 2D graphene nanosheets is expected to reduce the electron-hole recombination in niobate molecular sheet, leading to enhanced photocatalytic activity. Indeed, though MoS$_2$ exhibited negligible photocatalytic activity, the optimized H$_2$ evolution rates of MoS$_2$/niobate/TEOA/Graphene reached 2.12 mmol h^{-1} with methanol as a sacrificial reagent, which is much larger than that of niobate/TEOA alone.

It was demonstrated that the introduction of metal nanoparticles (Cr, Ag) to the surface of MoS$_2$ nanosheets could increase the photo-generated carrier separation and suppress the electron-hole recombination for HER applications [101]. The work function difference can drive electron transfer from Cr to MoS$_2$ to build an electric field at the thin metal/semiconductor interfacial barrier

layer (Fig. 14A), leading to an efficient separation of photo-generated carriers. This was supported by PL measurement, in which with MoS$_2$ as an electron sink, the intensity of the photoluminescence of Cr-MoS$_2$ hybrid nanosheets was extensively quenched. With Cr-MoS$_2$ as co-catalyst for CdS photocatalyst, the average rate of hydrogen evolution is 38,000 μmol g^{-1} h^{-1} under visible light with a sacrificial reagent, which is higher than that of MoS$_2$ as a single co-catalyst without Cr. Furthermore, significant enhancement is achieved for photocatalytic HER in the case of Ag-MoS$_2$ as co-catalyst, leading to an average rate of 107,000 μmol g^{-1} h^{-1}, which is six times higher than that of MoS$_2$ co-catalyst (Fig. 14B). Furthermore, the composite showed an excellent stability of 12 h against photocorrosion.

Perovskite-type SrZrO$_3$ with a band gap of 5.6 eV has been considered as a promising photocatalysts due to its high stability, more photocatalytic active sites and non-toxicity. Recently, Tian et al. [102] synthesized a novel heterojunction of a MoS$_2$/SrZrO$_3$ photocatalyst (via a simple hydrothermal process) and applied it for photocatalytic H$_2$ evolution under UV light irradiation. The rate of H$_2$ evolution for pure SrZrO$_3$ photocatalyst (with

Na$_2$S/Na$_2$SO$_3$ as a sacrificial agent) was 9.75 mmol h^{-1} g^{-1} whereas the rate was increased 2.7 times to reach 26.55 mmol h^{-1} g^{-1} by introducing 0.05 wt. % MoS$_2$ into SrZrO$_3$. The enhancement was attributed to the junction between SrZrO$_3$ and MoS$_2$, which can suppress the recombination of the photo-generated electron-hole.

In summary, the incorporation of metal nanoparticles (Cr, Ag) into MoS$_2$ can lead to the improvement in photocatalytic H$_2$ production, which is attributed to the reduction in photo-generated electron/hole recombination in MoS$_2$ nanosheets by Cr or Ag nanoparticles. Single molecular niobate sheets can facilitate the assembly with graphene, forming a promising MoS$_2$/niobate/TEOA/ Graphene photocatalyst, in which electrons can rapidly transfer from niobate nanosheets to MoS$_2$ through the 2D graphene nanosheets to reduce electron/hole recombination in niobate molecular sheets.

MoS$_2$/dye sensitizer

A molecular photon absorber, ruthenium trisbipyridine (Ru(bpy)$_3$), was added to colloid amorphous MoS$_2$ nanoparticles with diameter <10 nm [103]. With ascorbic acid as an electron donor, the HER activity of the colloidal system was evaluated under $\lambda > 420$ nm visible light, revealing the optimized H$_2$ yield of about 500 μmol H$_2$ with 12.5 μmol MoS$_2$ in 6 h. Furthermore, colloidal MoS$_2$ nanoparticles (NPs) were also combined with a series of cyclometalated Ir (III) sensitizers for multicomponent photocatalytic water reduction systems [77]. The existence of metal-carbon sigma bonds in cyclometalated Ir (III) emissive species improves their photostability compared to Ru(II) diimines under light illumination. The introduction of the carboxylate anchoring groups in the iridium complexes can allow the species to be chemically adsorbed onto MoS$_2$ NPs for the increase in electron transfer, resulting in enhancement of H$_2$ evolution. The highest apparent quantum yield was as high as 12.4% for H$_2$ evolution at $\lambda = 400$ nm with triethanolamine (TEOA) as an electron-donating agent, indicating that the combination between MoS$_2$ and dyes provides a promising approach to improve the photocatalytic activity of MoS$_2$.

Outlook

As a repressive layered transition metal dichalcogenides (TMDs), MoS$_2$ has been widely investigated as a co-catalyst for the photocatalytic hydrogen from water. Its combination with various other materials, such as CdS, graphene, and TiO$_2$, exhibited excellent photocatalytic performance. It is still an important topic to find new MoS$_2$-based

composite materials. For example, it was theoretically predicted that MoS$_2$ and AlN(GaN) can form an van der Waals (vdW) heterostructured composite as an efficient photocatalyst for water splitting under visible light irradiation [128]. The MoS$_2$/AlN(GaN) vdW catalyst can be expected to separately produce hydrogen and oxygen at the opposite surfaces, where the photo-excited electrons transfer from AlN(GaN) to MoS$_2$ during the photocatalysis process.

Although bulk MoS$_2$ cannot evolve hydrogen under light illumination due to slightly more positive CB than that for the HER, its CB varies with the number of its layers. Therefore, it needs intensive research to explore a single layer or few-layer MoS$_2$ samples as a single catalyst with both functions of absorbing light and catalyzing HER. Furthermore, the band structure of MoS$_2$ may also be tuned by creating hybrid-layered structures with other TMDs, such as WS$_2$, MoSe$_2$, and WSe$_2$. The hybrid TMD materials would be promising photocatalysts.

Conflict of Interest

None declared.

References

1. Lewis, N. S., and D. G. Nocera. 2006. Powering the planet: chemical challenges in solar energy utilization. Proc. Natl Acad. Sci. USA 103:15729–15735.

2. PE United Nations Department of Economic and Social Affairs, Population Division. July 2015. Available at: https://esa.un.org/unpd/wpp/Publications/Files/ Key_Findings_WPP_2015.pdf

3. Wang, H., and Y. H. Hu. 2012. Graphene as a counter electrode material for dye-sensitized solar cells. Energy Environ. Sci. 5:8182–8188.

4. Wei, W., H. Wang, and Y. H. Hu. 2013. Unusual particle-size-induced promoter-to-poison transition of ZrN in counter electrodes for dye-sensitized solar cells. J. Mater. Chem. A 1:14350–14357.

5. Wang, H., W. Wei, and Y. H. Hu. 2013. Efficient ZnO-based counter electrodes for dye-sensitized solar cells. J. Mater. Chem. A 1:607–611.

6. Crabtree, G., and N. Lewis. 2007. Solar energy conversion. Phys. Today 60:37–42.

7. Kudo, A., and Y. Miseki. 2009. Heterogeneous photocatalyst materials for water splitting. Chem. Soc. Rev. 38:253–278.

8. Walter, M. G., E. L. Warren, J. R. McKone, S. W. Boettcher, Q. Mi, E. A. Santori, et al. 2010. Solar water splitting cells. Chem. Rev. 110:6446–6473.

9. Fujishima, A., and K. Honda. 1972. Electrochemical photolysis of water at a semiconductor electrode. Nature 238:37–38.

10. Khaselev, O., and J. A. Turner. 1998. A monolithic photovoltaic-photoelectrochemical device for hydrogen production via water splitting. Science 280:425–427.

11. Khan, S. U. M., and J. Akikusa. 1999. Photoelectrochemical splitting of water at nanocrystalline N-Fe$_2$O$_3$ thin-film electrodes. J. Phys. Chem. B 103:7184–7189.

12. Santato, C., M. Ulmann, and J. Augustynski. 2001. Photoelectrochemical properties of nanostructured tungsten trioxide films. J. Phys. Chem. B 105:936–940.

13. Hou, Y., Abrams, B., Vesborg, P., Björketun, M., Herbst, K., Bech, L. 2011. Bioinspired molecular co-catalysts bonded to a silicon photocathode for solar hydrogen evolution. Nat. Mater. 10:434–438.

14. Matsumura, M., Y. Saho, and H. Tsubomura. 1983. Photocatalytic hydrogen production from solutions of sulfite using platinized cadmium sulfide powder. J. Phys. Chem. 87:3807–3808.

15. Maruthamuthu, P., K. Gurunathan, E. Subramanian, and M. Ashokkumar. 1991. Photocatalytic activities of Bi$_2$O$_3$, WO$_3$, and Fe$_2$O$_3$: an assessment through decomposition of peroxomonosulfate in visible radiation. Bull. Chem. Soc. Jpn. 64:1933–1937.

16. Kato, H., K. Asakura, and A. Kudo. 2003. Highly efficient water splitting into H$_2$ and O$_2$ over lanthanum-doped NaTaO$_3$ photocatalysts with high crystallinity and surface nanostructure. J. Am. Chem. Soc. 125:3082–3089.

17. Ohno, T., L. Bai, T. Hisatomi, K. Maeda, and K. Domen. 2012. Photocatalytic water splitting using modified Gan: Zno solid solution under visible light: long-time operation and regeneration of activity. J. Am. Chem. Soc. 134:8254–8259.

18. Jia, Q., A. Iwase, and A. Kudo. 2014. BiVO4-Ru/ SrTiO3: Rh composite Z-Scheme photocatalyst for solar water splitting. Chem. Sci. 5:1513–1519.

19. Tsuji, I., H. Kato, and A. Kudo. 2006. Photocatalytic hydrogen evolution on ZnS−CuInS$_2$−AgInS$_2$ solid solution photocatalysts with wide visible light absorption bands. Chem. Mater. 18:1969–1975.

20. Han, B., and Y. H. Hu. 2015. Highly efficient temperature-induced visible light photocatalytic hydrogen production from water. J. Phys. Chem. C 119:18927–18934.

21. Han, B., W. Wei, L. Chang, P. Cheng, and Y. H. Hu. 2016. Efficient visible light photocatalytic CO$_2$ reforming of CH$_4$. ACS Catal. 6:494–497.

22. U.S. Geological Survey. 2011. Mineral commodity summaries. U.S. Geological Survey, Reston, VA.

23. McKone, J. R., B. F. Sadtler, C. A. Werlang, N. S. Lewis, and H. B. Gray. 2012. Ni–Mo nanopowders for efficient electrochemical hydrogen evolution. ACS Catal. 3:166–169.

24. Merki, D., and X. Hu. 2011. Recent developments of molybdenum and tungsten sulfides as hydrogen evolution catalysts. Energy Environ. Sci. 4:3878–3888.

25. Laursen, A. B., S. Kegnaes, S. Dahl, and I. Chorkendorff. 2012. Molybdenum sulfides-efficient and viable materials for electro – and photoelectrocatalytic hydrogen evolution. Energy Environ. Sci. 5:5577–5591.

26. Chhowalla, M., H. S. Shin, G. Eda, L.-J. Li, K. P. Loh, and H. Zhang. 2013. The chemistry of two-dimensional layered transition metal dichalcogenide nanosheets. Nat. Chem. 5:263–275.

27. Benck, J. D., T. R. Hellstern, J. Kibsgaard, P. Chakthranont, and T. F. Jaramillo. 2014. Catalyzing the hydrogen evolution reaction (Her) with molybdenum sulfide nanomaterials. ACS Catal. 4:3957–3971.

28. Morales-Guio, C. G., and X. Hu. 2014. Amorphous molybdenum sulfides as hydrogen evolution catalysts. Acc. Chem. Res. 47:2671–2681.

29. Morales-Guio, C. G., L.-A. Stern, and X. Hu. 2014. Nanostructured hydrotreating catalysts for electrochemical hydrogen evolution. Chem. Soc. Rev. 43:6555–6569.

30. Yan, Y., B. Xia, Z. Xu, and X. Wang. 2014. Recent development of molybdenum sulfides as advanced electrocatalysts for hydrogen evolution reaction. ACS Catal. 4:1693–1705.

31. Zou, X., and Y. Zhang. 2015. Noble metal-free hydrogen evolution catalysts for water splitting. Chem. Soc. Rev. 44:5148–5180.

32. Li, S.-L., K. Tsukagoshi, E. Orgiu, and P. Samori. 2016. Charge transport and mobility engineering in two-dimensional transition metal chalcogenide semiconductors. Chem. Soc. Rev. 45:118–151.

33. Mak, K. F., and J. Shan. 2016. Photonics and optoelectronics of 2D semiconductor transition metal dichalcogenides. Nat. Photonics 10:216–226.

34. Dickinson, R. G., and L. Pauling. 1923. The crystal structure of molybdenite. J. Am. Chem. Soc. 45:1466–1471.

35. Frindt, R. F. 1966. Single crystals of MoS$_2$ several molecular layers thick. J. Appl. Phys. 37:1928–1929.

36. Joensen, P., R. F. Frindt, and S. R. Morrison. 1986. Single-layer MoS$_2$. Mater. Res. Bull. 21:457–461.

37. Koma, A., and K. Yoshimura. 1986. Ultrasharp interfaces grown with van der Waals epitaxy. Surf. Sci. 174:556–560.

38. Yang, D., S. J. Sandoval, W. M. R. Divigalpitiya, J. C. Irwin, and R. F. Frindt. 1991. Structure of single-molecular-layer MoS$_2$. Phys. Rev. B 43:12053–12056.

39. Late, D. J., B. Liu, H. S. S. R. Matte, V. P. Dravid, and C. N. R. Rao. 2012. Hysteresis in single-layer MoS$_2$ field effect transistors. ACS Nano 6:5635–5641.

40. Ataca, C., M. Topsakal, E. Aktürk, and S. Ciraci. 2011. A comparative study of lattice dynamics of three- and two-dimensional MoS$_2$. J. Phys. Chem. C 115:16354–16361.

41. Ataca, C., H. Şahin, and S. Ciraci. 2012. Stable, single-layer MX_2 transition-metal oxides and dichalcogenides in a honeycomb-like structure. J. Phys. Chem. C 116:8983–8999.

42. Beal, A. R., J. C. Knights, and W. Y. Liang. 1972. Transmission spectra of some transition metal dichalcogenides. II. Group via: trigonal prismatic coordination. J. Phys. C: Solid State Phys. 5:3540.

43. Shirodkar, S. N., and U. V. Waghmare. 2014. Emergence of ferroelectricity at a metal-semiconductor transition in a 1T monolayer of MoS_2. Phys. Rev. Lett. 112:157601.

44. Acerce, M., D. Voiry, and M. Chhowalla. 2015. Metallic 1t phase MoS_2 nanosheets as supercapacitor electrode materials. Nat. Nanotechnol. 10:313–318.

45. Cheng, P., K. Sun, and Y. H. Hu. 2016. Memristive behavior and ideal memristor of 1T phase MoS_2 nanosheets. Nano Lett. 16:572–576.

46. Cheng, P., K. Sun, and Y. H. Hu. 2016. Mechanically-induced reverse phase transformation of MoS_2 from stable 2H to metastable 1T and its memristive behavior. RSC Adv. 6:65691–65697.

47. Kuc, A. 2015. Low-dimensional transition-metal dichalcogenides. Pp. 1–29 in M. Springborg, and J. Joswig, ed. Chemical modelling: volume 11. The Royal Society of Chemistry, London, UK.

48. Xiang, Q., J. Yu, and M. Jaroniec. 2012. Synergetic effect of MoS_2 and graphene as cocatalysts for enhanced photocatalytic H₂ production activity of TiO_2 nanoparticles. J. Am. Chem. Soc. 134:6575–6578.

49. Kadantsev, E. S., and P. Hawrylak. 2012. Electronic structure of a single MoS_2 monolayer. Solid State Commun. 152:909–913.

50. Lee, H. S., S.-W. Min, Y.-G. Chang, M. K. Park, T. Nam, H. Kim, et al. 2012. MoS_2 nanosheet phototransistors with thickness-modulated optical energy gap. Nano Lett. 12:3695–3700.

51. Mak, K. F., C. Lee, J. Hone, J. Shan, and T. F. Heinz. 2010. Atomically thin MoS_2: a new direct-gap semiconductor. Phys. Rev. Lett. 105:136805.

52. Lee, C., H. Yan, L. E. Brus, T. F. Heinz, J. Hone, and S. Ryu. 2010. Anomalous lattice vibrations of single- and few-layer MoS_2. ACS Nano 4:2695–2700.

53. Ellis, J. K., M. J. Lucero, and G. E. Scuseria. 2011. The indirect to direct band gap transition in multilayered MoS_2 as predicted by screened hybrid density functional theory. Appl. Phys. Lett. 99:261908.

54. Kuc, A., N. Zibouche, and T. Heine. 2011. Influence of quantum confinement on the electronic structure of the transition metal sulfide TS_2. Phys. Rev. B 83:245213.

55. Eda, G., H. Yamaguchi, D. Voiry, T. Fujita, M. Chen, and M. Chhowalla. 2011. Photoluminescence from chemically exfoliated MoS_2. Nano Lett. 11:5111–5116.

56. Splendiani, A., L. Sun, Y. Zhang, T. Li, J. Kim, C.-Y. Chim, et al. 2010. Emerging photoluminescence in monolayer MoS_2. Nano Lett. 10:1271–1275.

57. Wilcoxon, J. P. 2000. Catalytic photooxidation of pentachlorophenol using semiconductor nanoclusters. J. Phys. Chem. B 104:7334–7343.

58. Rao, C. N. R., H. S. S. Ramakrishna Matte, and U. Maitra. 2013. Graphene analogues of inorganic layered materials. Angew. Chem. Int. Ed. 52:13162–13185.

59. Novoselov, K. S., D. Jiang, F. Schedin, T. J. Booth, V. V. Khotkevich, S. V. Morozov, et al. 2005. Two-dimensional atomic crystals. Proc. Natl Acad. Sci. USA 102:10451–10453.

60. Li, H., Z. Yin, Q. He, H. Li, X. Huang, G. Lu, et al. 2012. Fabrication of single- and multilayer MoS_2 film-based field-effect transistors for sensing no at room temperature. Small 8:63–67.

61. Coleman, J. N., et al. 2011. Two-dimensional nanosheets produced by liquid exfoliation of layered materials. Science 331:568–571.

62. Zhou, K.-G., N.-N. Mao, H.-X. Wang, Y. Peng, and H.-L. Zhang. 2011. A mixed-solvent strategy for efficient exfoliation of inorganic graphene analogues. Angew. Chem. Int. Ed. 50:10839–10842.

63. Wang, X., H. Feng, Y. Wu, and L. Jiao. 2013. Controlled synthesis of highly crystalline MoS_2 flakes by chemical vapor deposition. J. Am. Chem. Soc. 135:5304–5307.

64. Huang, X., Z. Zeng, and H. Zhang. 2013. Metal dichalcogenide nanosheets: preparation, properties and applications. Chem. Soc. Rev. 42:1934–1946.

65. Ramakrishna Matte, H. S. S., A. Gomathi, A. K. Manna, D. J. Late, R. Datta, S. K. Pati, et al. 2010. MoS_2 and WS_2 analogues of graphene. Angew. Chem. Int. Ed. 49:4059–4062.

66. Altavilla, C., M. Sarno, and P. Ciambelli. 2011. A novel wet chemistry approach for the synthesis of hybrid 2D free-floating single or multilayer nanosheets of MS_2@Oleylamine (M=Mo, W). Chem. Mater. 23:3879–3885.

67. Peng, Y., Z. Meng, C. Zhong, J. Lu, W. Yu, Y. Jia, et al. 2001. Hydrothermal synthesis and characterization of single-molecular-layer MoS_2 and $MoSe_2$. Chem. Lett. 30:772–773.

68. Zong, X., H. Yan, G. Wu, G. Ma, F. Wen, L. Wang, et al. 2008. Enhancement of photocatalytic H₂ evolution on CdS by loading MoS_2 as cocatalyst under visible light irradiation. J. Am. Chem. Soc. 130:7176–7177.

69. Liu, Y., H. Yu, X. Quan, and S. Chen. 2013. Green synthesis of feather-shaped MoS_2/CdS photocatalyst for effective hydrogen production. Int. J. Photoenergy 2013, 247516–247521.

70. Chen, G., D. Li, F. Li, Y. Fan, H. Zhao, Y. Luo, et al. 2012. Ball-milling combined calcination synthesis of MoS_2/CdS photocatalysts for high photocatalytic H₂

evolution activity under visible light irradiation. Appl. Catal. A 443–444:138–144.

71. Kanda, S., T. Akita, M. Fujishima, and H. Tada. 2011. Facile synthesis and catalytic activity of MoS$_2$/TiO$_2$ by a photodeposition-based technique and its oxidized derivative MoO$_3$/TiO$_2$ with a unique photochromism. J. Colloid Interface Sci. 354:607–610.

72. Zhuo, S., Y. Xu, W. Zhao, J. Zhang, and B. Zhang. 2013. Hierarchical nanosheet-based MoS$_2$ nanotubes fabricated by an anion-exchange reaction of MoO$_3$–amine hybrid nanowires. Angew. Chem. Int. Ed. 52:8602–8606.

73. Maitra, U., U. Gupta, M. De, R. Datta, A. Govindaraj, and C. N. R. Rao. 2013. Highly effective visible-light-induced H$_2$ generation by single-layer 1t-MoS$_2$ and a nanocomposite of few-layer 2H-MoS$_2$ with heavily nitrogenated graphene. Angew. Chem. Int. Ed. 52:13057–13061.

74. Popczun, E. J., J. R. McKone, C. G. Read, A. J. Biacchi, A. M. Wiltrout, N. S. Lewis, et al. 2013. Nanostructured nickel phosphide as an electrocatalyst for the hydrogen evolution reaction. J. Am. Chem. Soc. 135:9267–9270.

75. Popczun, E. J., C. G. Read, C. W. Roske, N. S. Lewis, and R. E. Schaak. 2014. Highly active electrocatalysis of the hydrogen evolution reaction by cobalt phosphide nanoparticles. Angew. Chem. Int. Ed. 53:5427–5430.

76. Jaramillo, T. F., K. P. Jørgensen, J. Bonde, J. H. Nielsen, S. Horch, and I. Chorkendorff. 2007. Identification of active edge sites for electrochemical H$_2$ evolution from MoS$_2$ nanocatalysts. Science 317:100–102.

77. Yuan, Y.-J., Z.-T. Yu, X.-J. Liu, J.-G. Cai, Z.-J. Guan, and Z.-G. Zou. 2014. Hydrogen photogeneration promoted by efficient electron transfer from iridium sensitizers to colloidal MoS$_2$ catalysts. Sci. Rep. 4:4045–4054.

78. Wang, Z., J. Hou, C. Yang, S. Jiao, and H. Zhu. 2014. Three-dimensional MoS$_2$-Cds-[Gamma]-Taon hollow composites for enhanced visible-light-driven hydrogen evolution. Chem. Commun. 50:1731–1734.

79. Zhang, J., Z. Zhu, and X. Feng. 2014. Construction of two-dimensional MoS2/Cds P-N nanohybrids for highly efficient photocatalytic hydrogen evolution. Chemistry 20:10632–10635.

80. Li, Y., H. Wang, and S. Peng. 2014. Tunable photodeposition of MoS$_2$ onto a composite of reduced graphene oxide and Cds for synergic photocatalytic hydrogen generation. J. Phys. Chem. C 118:19842–19848.

81. Xu, J., and X. Cao. 2015. Characterization and mechanism of MoS$_2$/Cds composite photocatalyst used for hydrogen production from water splitting under visible light. Chem. Eng. J. 260:642–648.

82. Min, S., and G. Lu. 2012. Sites for high efficient photocatalytic hydrogen evolution on a limited-layered

MoS$_2$ cocatalyst confined on graphene sheets-the role of graphene. J. Phys. Chem. C 116:25415–25424.

83. Meng, F., J. Li, S. K. Cushing, M. Zhi, and N. Wu. 2013. Solar hydrogen generation by nanoscale p–n junction of P-type molybdenum disulfide/N-type nitrogen-doped reduced graphene oxide. J. Am. Chem. Soc. 135:10286–10289.

84. Liu, M., F. Li, Z. Sun, L. Ma, L. Xu, and Y. Wang. 2014. Noble-metal-free photocatalysts MoS$_2$-graphene/Cds mixed nanoparticles/nanorods morphology with high visible light efficiency for H$_2$ evolution. Chem. Commun. 50:11004–11007.

85. Chang, K., Z. Mei, T. Wang, Q. Kang, S. Ouyang, and J. Ye. 2014. MoS$_2$/graphene cocatalyst for efficient photocatalytic H$_2$ evolution under visible light irradiation. ACS Nano 8:7078–7087.

86. Latorre-Sánchez, M., I. Esteve-Adell, A. Primo, and H. García. 2015. Innovative preparation of MoS$_2$–graphene heterostructures based on alginate containing (NH$_4$)$_2$MoS$_4$ and their photocatalytic activity for H$_2$ generation. Carbon 81:587–596.

87. Djamil, J., S. A. Segler, A. Dabrowski, W. Bensch, A. Lotnyk, U. Schurmann, et al. 2013. The influence of carbon content on the structure and properties of mosxcy photocatalysts for light-driven hydrogen generation. Dalton Trans. 42:1287–1292.

88. Frame, F. A., and F. E. Osterloh. 2010. Cdse-MoS$_2$: a quantum size-confined photocatalyst for hydrogen evolution from water under visible light. J. Phys. Chem. C 114:10628–10633.

89. Sobczynski, A. 1991. Molybdenum disulfide as a hydrogen evolution catalyst for water photodecomposition on semiconductors. J. Catal. 131:156–166.

90. Zhou, W., Z. Yin, Y. Du, X. Huang, Z. Zeng, Z. Fan, et al. 2013. Synthesis of few-layer MoS$_2$ nanosheet-coated TiO$_2$ nanobelt heterostructures for enhanced photocatalytic activities. Small 9:140–147.

91. Liu, Q., Z. Pu, A. Asiri, A. Qusti, A. Al-Youbi, and X. Sun. 2013. One-step solvothermal synthesis of MoS$_2$/TiO$_2$ nanocomposites with enhanced photocatalytic H$_2$ production. J. Nanopart. Res. 15:1–7.

92. Zhu, Y., Q. Ling, Y. Liu, H. Wang, and Y. Zhu. 2015. Photocatalytic H$_2$ evolution on MoS$_2$-TiO$_2$ catalysts synthesized via mechanochemistry. Phys. Chem. Chem. Phys. 17:933–940.

93. Liu, C., L. Wang, Y. Tang, S. Luo, Y. Liu, S. Zhang, et al. 2015. Vertical single or few-layer MoS$_2$ nanosheets rooting into TiO$_2$ nanofibers for highly efficient photocatalytic hydrogen evolution. Appl. Catal. B 164:1–9.

94. Ge, L., C. Han, X. Xiao, and L. Guo. 2013. Synthesis and characterization of composite visible light active photocatalysts MoS$_2$–g-C$_3$N$_4$ with enhanced hydrogen

evolution activity. Int. J. Hydrogen Energy 38:6960–6969.

95. Hou, Y., A. B. Laursen, J. Zhang, G. Zhang, Y. Zhu, X. Wang, et al. 2013. Layered nanojunctions for hydrogen-evolution catalysis. Angew. Chem. Int. Ed. 52:3621–3625.

96. Wei, L., Y. Chen, Y. Lin, H. Wu, R. Yuan, and Z. Li. 2014. MoS$_2$ as non-noble-metal co-catalyst for photocatalytic hydrogen evolution over hexagonal Znin2s4 under visible light irradiations. Appl. Catal. B 144:521–527.

97. Chen, G., N. Ding, F. Li, Y. Fan, Y. Luo, D. Li, et al. 2014. Enhancement of photocatalytic H$_2$ evolution on ZnIn$_2$S$_4$ loaded with in-situ photo-deposited MoS$_2$ under visible light irradiation. Appl. Catal. B 160–161:614–620.

98. Zhu, B., B. Lin, Y. Zhou, P. Sun, Q. Yao, Y. Chen, et al. 2014. Enhanced photocatalytic H$_2$ evolution on ZnS loaded with graphene and MoS$_2$ nanosheets as cocatalysts. J. Mater. Chem. A 2:3819–3827.

99. Tang, M. L., D. C. Grauer, B. Lassalle-Kaiser, V. K. Yachandra, L. Amirav, J. R. Long, et al. 2011. Structural and electronic study of an amorphous MoS$_3$ hydrogen-generation catalyst on a quantum-controlled photosensitizer. Angew. Chem. Int. Ed. 50:10203–10207.

100. Nakagawa, K., T. Jia, W. Zheng, S. M. Fairclough, M. Katoh, S. Sugiyama, et al. 2014. Enhanced photocatalytic hydrogen evolution from water by niobate single molecular sheets and ensembles. Chem. Commun. 50:13702–13705.

101. Yang, L., et al. 2014. Optical properties of metal–molybdenum disulfide hybrid nanosheets and their application for enhanced photocatalytic hydrogen evolution. ACS Nano 8:6979–6985.

102. Tian, Q., L. Zhang, J. Liu, N. Li, Q. Ma, J. Zhou, et al. 2015. Synthesis of MoS$_2$/SrZrO$_3$ heterostructures and their photocatalytic H2 evolution under UV irradiation. RSC Adv. 5:734–739.

103. Zong, X., Y. Na, F. Wen, G. Ma, J. Yang, D. Wang, et al. 2009. Visible light driven H$_2$ production in molecular systems employing colloidal MoS$_2$ nanoparticles as catalyst. Chem. Commun. 30:4536–4538.

104. Shen, M., Z. Yan, L. Yang, P. Du, J. Zhang, and B. Xiang. 2014. MoS$_2$ nanosheet/TiO$_2$ nanowire hybrid nanostructures for enhanced visible-light photocatalytic activities. Chem. Commun. 50:15447–15449.

105. Yoon, Y., K. Ganapathi, and S. Salahuddin. 2011. How good can monolayer MoS$_2$ transistors be? Nano Lett. 11:3768–3773.

106. Zong, X., G. Wu, H. Yan, G. Ma, J. Shi, F. Wen, et al. 2010. Photocatalytic H$_2$ evolution on MoS$_2$/Cds catalysts under visible light irradiation. J. Phys. Chem. C 114:1963–1968.

107. Liu, Y., Y.-X. Yu, and W.-D. Zhang. 2013. MoS$_2$/Cds heterojunction with high photoelectrochemical activity for H$_2$ evolution under visible light: the role of MoS$_2$. J. Phys. Chem. C 117:12949–12957.

108. Raja, R., P. Sudhagar, A. Devadoss, C. Terashima, L. K. Shrestha, K. Nakata, et al. 2015. Pt-free solar driven photoelectrochemical hydrogen fuel generation using 1t MoS$_2$ co-catalyst assembled Cds Qds/TiO$_2$ photoelectrode. Chem. Commun. 51:522–525.

109. Novoselov, K. S., A. K. Geim, S. V. Morozov, D. Jiang, Y. Zhang, S. V. Dubonos, et al. 2004. Electric field effect in atomically thin carbon films. Science 306:666–669.

110. Hu, Y. H., H. Wang, and B. Hu. 2010. Thinnest two-dimensional nanomaterial—graphene for solar energy. ChemSusChem 3:782.

111. Xiang, Q., J. Yu, and M. Jaroniec. 2012. Graphene-based semiconductor photocatalysts. Chem. Soc. Rev. 41:782–796.

112. Gao, W., M. Wang, C. Ran, and L. Li. 2015. Facile one-pot synthesis of MoS$_2$ quantum dots-graphene-TiO$_2$ composites for highly enhanced photocatalytic properties. Chem. Commun. 51:1709–1712.

113. Li, Y., H. Wang, L. Xie, Y. Liang, G. Hong, and H. Dai. 2011. MoS$_2$ Nanoparticles grown on graphene: an advanced catalyst for the hydrogen evolution reaction. J. Am. Chem. Soc. 133:7296–7299.

114. Wang, X., K. Maeda, A. Thomas, K. Takanabe, G. Xin, J. M. Carlsson, et al. 2009. A metal-free polymeric photocatalyst for hydrogen production from water under visible light. Nat. Mater. 8:76–80.

115. Zhang, J., X. Chen, K. Takanabe, K. Maeda, K. Domen, J. D. Epping, et al. 2010. Synthesis of a carbon nitride structure for visible-light catalysis by copolymerization. Angew. Chem. Int. Ed. 49:441–444.

116. Lunt, R. R., K. Sun, M. Kröger, J. B. Benziger, and S. R. Forrest. 2011. Ordered organic-organic multilayer growth. Phys. Rev. B 83:064114.

117. Hong, Y. J., and T. Fukui. 2011. Controlled Van Der Waals heteroepitaxy of Inas nanowires on carbon honeycomb lattices. ACS Nano 5:7576–7584.

118. Kibsgaard, J., Z. Chen, B. N. Reinecke, and T. F. Jaramillo. 2012. Engineering the surface structure of MoS$_2$ to preferentially expose active edge sites for electrocatalysis. Nat. Mater. 11:963–969.

119. Hu, S. W., L. W. Yang, Y. Tian, X. L. Wei, J. W. Ding, J. X. Zhong, et al. 2014. Non-covalent doping of graphitic carbon nitride with ultrathin graphene oxide and molybdenum disulfide nanosheets: an effective binary heterojunction photocatalyst under visible light irradiation. J. Colloid Interface Sci. 431:42–49.

120. Wang, J., Z. Guan, J. Huang, Q. Li, and J. Yang. 2014. Enhanced photocatalytic mechanism for the

hybrid g-C$_3$N$_4$/MoS$_2$ nanocomposite. J. Mater. Chem. A 2:7960–7966.

121. Gratzel, M. 2001. Photoelectrochemical cells. Nature 414:338–344.

122. Meng, C., Z. Liu, T. Zhang, and J. Zhai. 2015. Layered MoS$_2$ nanoparticles on TiO$_2$ nanotubes by a photocatalytic strategy for use as high-performance electrocatalysts in hydrogen evolution reactions. Green Chem. 17:2764–2768.

123. Zhang, J., J. Yu, Y. Zhang, Q. Li, and J. R. Gong. 2011. Visible light photocatalytic H$_2$-production activity of CuS/ZnS porous nanosheets based on photoinduced interfacial charge transfer. Nano Lett. 11:4774–4779.

124. Zhang, Y., N. Zhang, Z.-R. Tang, and Y.-J. Xu. 2012. Graphene transforms wide band Gap ZnS to a visible light photocatalyst. The new role of graphene as a macromolecular photosensitizer. ACS Nano 6:9777–9789.

125. Reber, J. F., and K. Meier. 1984. Photochemical production of hydrogen with zinc sulfide suspensions. J. Phys. Chem. 88:5903–5913.

126. Zhang, K., and L. Guo. 2013. Metal sulphide semiconductors for photocatalytic hydrogen production. Catal. Sci. Technol. 3:1672–1690.

127. Thurston, T. R., and J. P. Wilcoxon. 1998. Photooxidation of organic chemicals catalyzed by nanoscale MoS$_2$. J. Phys. Chem. B 103:11–17.

128. Liao, J., B. Sa, J. Zhou, R. Ahuja, and Z. Sun. 2014. Design of high-efficiency visible-light photocatalysts for water splitting: MoS$_2$/Aln(Gan) heterostructures. J. Phys. Chem. C 118:17594–17599.

129. Jia, T., A. Kolpin, C. Ma, R. C.-T. Chan, W.-M. Kwok, and S. C. E. Tsang. 2014. A graphene dispersed Cds-MoS$_2$ nanocrystal ensemble for cooperative photocatalytic hydrogen production from water. Chem. Commun. 50:1185–1188.